International Journal of Multiphase Flow 120 (2019) 103103

Contents lists available at ScienceDirect

International Journal of Multiphase Flow

journal homepage: www.elsevier.com/locate/ijmulflow

On the role of the surface rheology in film drainage between fluid particles

Suat Canberk Ozan*, Hugo Atle Jakobsen

Department of Chemical Engineering, Norwegian University of Science and Technology (NTNU), Trondheim N- 7491, Norway

ARTICLE INFO

Article history:
Received 13 June 2019
Revised 26 August 2019
Accepted 28 August 2019
Available online 4 September 2019

Keywords:
Film drainage
Coalescence time
Approach velocity
Surface viscosity
Boussinesq surface fluid
Marangoni flow

ABSTRACT

Coalescence in the presence of low surfactant concentrations is investigated via a film drainage model, where the interface is a Boussinesq surface fluid with surfactant concentration dependent physical properties. Three cases are considered representing the systems where water is the continuous phase and the dispersed phase is either high viscosity droplets, droplets of comparable viscosity to water or gas bubbles. In the former, the immobilization of the interface is due to high dispersed phase viscosity and surface viscosities, whereas in the latter two, the Marangoni flow plays an important role, too. When droplets of comparable viscosity to water or gas bubbles are considered, it is seen that both the Marangoni flow and the surface viscosities can change the coalescence time significantly for the experimentally encountered values of the initial surfactant concentration, and the Boussinesq and surface Péclet numbers. In all cases, the impact of the surface phenomena amplifies with the approach velocity, especially for the dimpled interfaces. A complete immobilization criterion that is independent of the dispersed phase viscosity is proposed as a function of the continuous phase and surface viscosities, and the particle radii.

1. Introduction

Efficient operation of many engineering units, such as chemical and biochemical reactors or separators, requires precise understanding on the nature of the multiphase flow within them. The flow in such units is often characterized by the size and the distribution of the fluid particles dispersed in the continuous phase, which depend strongly on the coalescence and the breakage of the particles. Thus, these phenomena should be studied both on the equipment scale, where a large number of fluid particles interact simultaneously, and on an individual level, where a single event of coalescence or breakage is considered. This work focuses on the latter, more specifically, on the significance of the surface tension driven flows along the interface and the surface viscosities on the coalescence of two fluid particles.

Following Liao and Lucas (2010), the physical models describing the coalescence probability of interacting fluid particles can be summarized under three approaches. The film drainage approach starts with the studies of Shinnar and Church (1960), and Shinnar (1961), where they observe the emergence of a thin film in between the fluid particles once they are brought into contact. As the emergent thin film has to be drained before the coalescence, it delays the process, and thus, immediate coalescence is rarely seen. On the other hand, Howarth (1964) concludes that there exists a critical particle approach velocity distinguishing between two different regimes, where higher approach velocities result in rapid coalescence, and for lower values coalescence is unlikely. This conclusion forms the basis of the energy models, where the coalescence efficiency is expressed in terms of the kinetic energy of the colliding particles and the interfacial energy of the fluid particles. The third approach arises from the experimental findings of Lehr et al. (2002), where they observe a new regime in which the particles bounce instead of coalescing rapidly. As the critical velocity of Howarth (1964) indicates the beginning of the immediate coalescence, and the one of Lehr et al. (2002) is defined at the end of the same regime, it can be claimed that the latter corresponds to higher approach velocities than the former. Similar critical approach velocities to that of Lehr et al. (2002) are proposed by Kirkpatrick and Lockett (1974), and Chesters and Hofman (1982) in their theoretical works via a film drainage model and energy considerations, respectively. This implies that although all three approaches are given through different arguments, they might yield similar conclusions.

The film drainage approach uses two characteristic time scales to estimate the coalescence probability after collision: the con-

* Corresponding author.
E-mail address: canberk.ozan@ntnu.no (S.C. Ozan).

https://doi.org/10.1016/j.ijmultiphaseflow.2019.103103

tact time of the particles and the time required for coalescence. Furthermore, it is assumed that the coalescence process has two consecutive steps after the formation of the thin film. First, the thin film drains until its thickness reaches to a critical value, and then, the film ruptures and coalescence occurs. Since the drainage time is typically much larger than the time of rupture, the coalescence time is often approximated as the drainage time. Then, an expression for the coalescence efficiency λ_c is proposed by Coulaloglou (1975) as

$$\lambda_c = exp\left(-\frac{t_{drainage}}{t_{contact}}\right) \tag{1}$$

Thus, there has been extensive efforts on the models estimating the drainage time in the literature. One popular type of approach employs the lubrication equations, in which the thin film is treated as having a disc-like shape and the interfaces as being either flat or very close to flat. The flow in the film is given as the sum of two contributions, the parabolic and the plug components, which are driven by the pressure gradient within the film and the tangential speed of the interface, respectively (Lee and Hodgson, 1968). In this class of models, the deformability and the tangential mobility of the interface also play key roles as discussed by Lee and Hodgson (1968), Chesters (1991) and Liao and Lucas (2010). The models considering deformable interfaces are capable of simulating the dimple formation, which is frequently observed in experimental studies (Derjaguin and Kussakov, 1939; Allan et al., 1961; Klaseboer et al., 2000). Its tangential mobility, on the other hand, result in the classification of the interface as immobile, partially mobile or fully mobile (Chesters, 1991; Liao and Lucas, 2010). The primary reasons behind the immobilization of the interface are usually considered as high dispersed phase viscosities and the presence of surfactants at the interface (Lee and Hodgson, 1968). Regardless of the immobilization mechanism, the models with immobile interfaces neglect the tangential velocity of the interface and the plug component of the film flow. Davis et al. (1989) carry out a dimensional analysis on the characteristic scales governing the coalescence, and defines a measure of the interface mobility, m, which is inversely proportional to the dispersed to continuous phase viscosity ratio. According to their definition, when $m \approx 1$ the interface is partially mobile and when $m >> 1$ its fully mobile. On the other hand, Chesters (1991) emphasizes the treatment of the tangential stress at the interface to define the same concepts: zero tangential stress corresponds to inertial collision/film drainage and the interface is said to be fully mobile, whereas for partially mobile interfaces the stress is non-zero and the drainage is controlled by the dispersed phase viscosity.

First proposed by Davis et al. (1989), the determination of the tangential velocity of the interface via the boundary integral form of the Stokes flow, has been preferred in many studies (Yiantsios and Davis, 1991; Abid and Chesters, 1994; Saboni et al., 1995; Klaseboer et al., 2000; Bazhlekov et al., 2000; Alexandrova, 2014; Ozan and Jakobsen, 2019). Yiantsios and Davis (1991) investigate the buoyancy driven interactions between two deformable fluid particles. They show that, as the strength of the van der Waals forces decreases, the location at which the rupture occurs shifts from the center of the axisymmetry to a rim emerging due to the dimple formation, i.e., the type of rupture shifts from being a nose rupture to a rim rupture. The constant approach velocity and the constant interaction force collisions in liquid-liquid systems are studied by Abid and Chesters (1994) and Saboni et al. (1995), respectively. In both studies, the film flow is driven only by the mobility of the interface and the parabolic component is neglected. Klaseboer et al. (2000) discuss two film drainage models, in which the interface is either immobile or mobile. In both models, the interface is deformable and the relative approach velocity of the particles throughout the collision is kept constant. They carry out a comparison between their experiments and the theoretical model predictions by tracking the minimum film thickness, the film thickness at the center of the film and the radial position of the rim, which reveals that the immobile model matches the experimental data more accurately. Bazhlekov et al. (2000) introduce the dispersed to continuous phase viscosity ratio to the thinning equation. The viscosity ratio weighs the parabolic component of the film flow and allows the investigation of different degrees of interfacial mobility, instead of the strictly mobile or immobile models previously used in the literature. Ozan and Jakobsen (2019) estimate the coalescence time as a function of the relative approach velocity and the viscosity ratio via a similar model, in which the van der Waals forces are also taken into account. They identify three consecutive regimes as the approach velocity increases. At lower velocities, the coalescence time decreases with the approach velocity. Here, the rupture is a nose rupture and the coalescence time is a power function of the velocity. Then, in the second regime, the dimple formation at the interface starts and the rupture position shifts to the rim. Consequently, the coalescence time continues to decrease with the approach velocity, but less and less dramatically as the velocity increases. In the beginning of the last regime, the coalescence time reaches a minimum value and starts to increase due to the emergence of additional rim-like structures at the interface. The power law type relation between the coalescence time and the approach velocity in the first regime and the minimum point in the second regime they observe, seem to agree with the findings of recent experimental studies carried out in air-liquid systems such as Del Castillo et al. (2011) and Orvalho et al. (2015). In addition, the values Ozan and Jakobsen (2019) determine via their simulations for the exponent of the power law type relation in the first region, match the value of -0.85 given by Orvalho et al. (2015). However, the experimental works do not report a trend similar to the third region seen in theoretical work of Ozan and Jakobsen (2019). This discrepancy may indicate that there are additional mechanisms playing key roles at higher velocities.

Alexandrova (2014) studies the effect of the presence of surfactants in droplet coalescence by introducing surfactant balance across the interface and surface tension gradients resulting in Marangoni type flows along the interface. In the physical system considered, the viscous effects in the thin film are neglected, and the interaction force between the droplets is constant. She concludes that as the Péclet number increases the rate of drainage slows down, and for its very high values no rims emerge at the interface. Li (1996) introduces the dilatational and the shear viscosities of the surface in the film drainage model by employing a linear Boussinesq surface fluid expression for the interface. However, his approach is different than the other works mentioned earlier, as the boundary integral method is not employed, and instead the bubble side tangential stress is neglected. Therefore, he is not able to extend the examination to droplets. In addition, the boundary conditions are applied at a predefined rim position, and consequently the model fails to capture the mechanics of the rim/dimple formation. He presents explicit expressions for the coalescence time as functions of various physical properties and the droplet size, which seem to fit some experimental results better than the preexisting models with immobile interfaces. In an earlier work, Zapryanov et al. (1983) investigate the effect of the interfacial properties on the drainage rate of a thin film between two droplets with non-deformable interfaces. They show that the surface viscosity increases the drainage time as it immobilizes the interface, but the effect of the Marangoni flow is much more pronounced. Additionally, they conclude that the surface viscosities affect the drainage only when they are in between $10^{-6} Pa \cdot m \cdot s$ and $10^{-3} Pa \cdot m \cdot s$. These limits correspond to $10^{-3}\, sp$ and $1\, sp$, respectively, where sp stands for surface Poise and is

equal to g/s. However, it is not easy to compare these values to real systems, as there is an ongoing disagreement in the literature on the measurements of the surface viscosities, mainly due to difficulties in isolating the effect of the surface viscosities from those of the bulk properties and Marangoni stresses (Shen et al., 2018). Djabbarah and Wasan (1982) report surface viscosities as large as $2\,sp$ in their experiments with aqueous sodium lauryl sulfate solutions. Ting et al. (1984) measure values up to $0.3\,sp$ for a similar system with aqueous solutions of octanoic acid. Both studies employ deep channel viscous traction viscometer (as described by Pintar et al., 1971) and longitudinal wave apparatus (as described by Maru and Wasan, 1979) to determine the shear and the dilatational surface viscosities, respectively. They conclude that the surface shear viscosity is orders of magnitudes smaller than the dilatational ones, whereas Edwards et al. (1991) argue that the shear and the dilatational components might be on the same order of magnitude. In a more recent study, Zell et al. (2014) use microbutton surface rheometry to create only surface shear deformations and conclude that the surface shear viscosity of sodium dodecyl sulfate monolayer is below the sensitivity of their measurement technique, which corresponds to $10^{-5}\,sp$, whereas they measure values as high as $10^{-1}\,sp$ for an insoluble monolayer of 1-eicosanol.

Some recent studies on thin films and on fluid particles revealed that the surface viscosities might be important under specific conditions, or in explaining some experimental observations that cannot be explained by other surface phenomena such as Marangoni flows. Scheid et al. (2010) examine the significance of surface viscosities in film coating, and shows that there is a new regime of film thickening governed by the surface viscosities instead of the Marangoni effects. In their study on the breakup of a pendant drop, Ponce-Torres et al. (2017), show that the addition of the surface viscosities in their model is a must to successfully simulate their experiments, where a large amount of surfactants accumulate in the satellite droplets. Shen et al. (2018) come to the conclusion that the critical wavelength of the capillary waves can be affected significantly even by small surface viscosities. All these recent findings naturally raise a question on the extent to which the surface viscosities has an effect on the coalescence of the fluid particles. Although, both the Marangoni stresses and the surface viscosities immobilize the interface, they achieve this through different mechanisms. The Marangoni stresses due to the surface tension gradients create local flows from low to high surface tension, whereas the surface viscosities' effect is twofold: they reduce the overall magnitude of the surface velocities and their gradients along the interface, and as they lower the gradient they weaken the Marangoni flows. Therefore, investigating the effect of the surface viscosities together with the Marangoni stresses might shed light on to the importance of the interfacial dynamics during coalescence.

In this work, we aim to simulate both liquid–liquid and gas–liquid systems, in which low amounts of surfactants are present. When non-uniformly distributed along the interface, the surfactants result in surface tension gradients and consequently Marangoni flow. Furthermore, regardless of the uniformity of the distribution, the surfactants might also affect the viscous properties of the interface. Both the surface viscosities and the Marangoni flow can immobilize the interface, and consequently affect the coalescence time drastically. To check the degree of their impact, we extend the model of Ozan and Jakobsen (2019) by introducing the surface excess concentration distribution along the interface, and a viscous interface represented by the Boussinesq surface fluid model with concentration dependent properties. We follow the same framework and examine the coalescence time as a function of the approach velocity of the particles, at various levels of initial surfactant concentration. The key parameters, the surface Péclet and the Boussinesq numbers, signify the ratio of convective to diffusive rate of transport along the interface, and the ratio of the surface viscous forces to their bulk counterparts, respectively. The analysis is carried out for three distinct cases based on the dispersed to continuous phase viscosity ratio to simulate the systems with: high droplet to water viscosity ratio, comparable droplet to water viscosity ratio, and gas bubbles in water. For all systems, the conditions under which the Marangoni flow and/or the surface viscosities affect the coalescence time, are determined in terms of the initial surfactant concentration, and the surface Péclet and the Boussinesq numbers. Finally, a limit for the interfaces' complete immobilization is identified as a function of the continuous phase and the surface viscosities.

The physical configuration and the corresponding mathematical model are presented in Section 2, followed by the numerical procedure in Section 3. The results and discussion are given in Section 4 and organized under three subtitles. The drainage without the coalescence is discussed in Section 4.1. In Section 4.2, the results for the coalescence of the droplets with high viscosity are shown. The results of the comparable droplet to water viscosity ratio and the gas bubbles in water cases are given together in Section 4.3, as the same model is used for both. Finally, the conclusions drawn throughout the study are summarized in Section 5.

2. Physical system and mathematical model

Fig. 1 depicts two particles of the same fluid, with radii R_1 and R_2, approaching each other at a constant relative approach velocity, V_{app}, along their centerlines through a continuous medium. Both the dispersed and the continuous phases are incompressible and Newtonian, characterized by the viscosities μ_d and μ_c, respectively. The interfaces are deformable and exhibit Newtonian behavior, i.e., they obey the Boussinesq surface fluid model. The surfactants present in the system are not soluble in the dispersed phase.

Three distinct length scales governing the phenomenon can be identified: the particle radii, the radius and the thickness of the film. The relation between the magnitudes of these characteristic lengths play a significant role in the interaction between the fluid particles. In this work, the collisions considered are gentle ones, and they result in formation of a thin film of the continuous phase in between the fluid particles. Here, a gentle collision refers to a collision where the radius of the emerging thin film is much smaller than the radii of the fluid particles; whereas the thin film indicates that the film thickness is much smaller than the film radius. For coalescence to occur, this thin film has to be drained until a critical thickness of the film is reached. Although, the particle sizes are allowed to be different, i.e., $R_1 \neq R_2$ is possible, the equivalent particle radius,

$$R_p = 2\left(\frac{1}{R_1} + \frac{1}{R_2}\right)^{-1} \tag{2}$$

can be used to characterize both particles, as the collision is a gentle one (Chesters, 1991). Following Ozan and Jakobsen (2019), the length scales governing the collision can be written in terms of the equivalent particle radius:

$$\bar{h} = \epsilon^2 R_p, \qquad \bar{r} = \epsilon R_p \tag{3}$$

where $\bar{h}$ and $\bar{r}$, the characteristic length scales for the thickness and the radius of the film, and the small parameter ϵ is defined as $\epsilon = \sqrt{\frac{\bar{h}}{R_p}}$. The introduction of R_p also suggests symmetry around r axis in addition to the inherent axisymmetry due to the centerline collision of the fluid particles, and creates four equivalent quadrants around rz coordinate system shown in Fig. 1. Due to the symmetric nature of the physical configuration, the problem is only solved in the $r \geq 0$, $z \geq 0$ quadrant, where the interface is represented by the axisymmetric surface $z = h(r,t)/2$. Following Appendix B of Johns and Narayanan (2007), such a surface can be

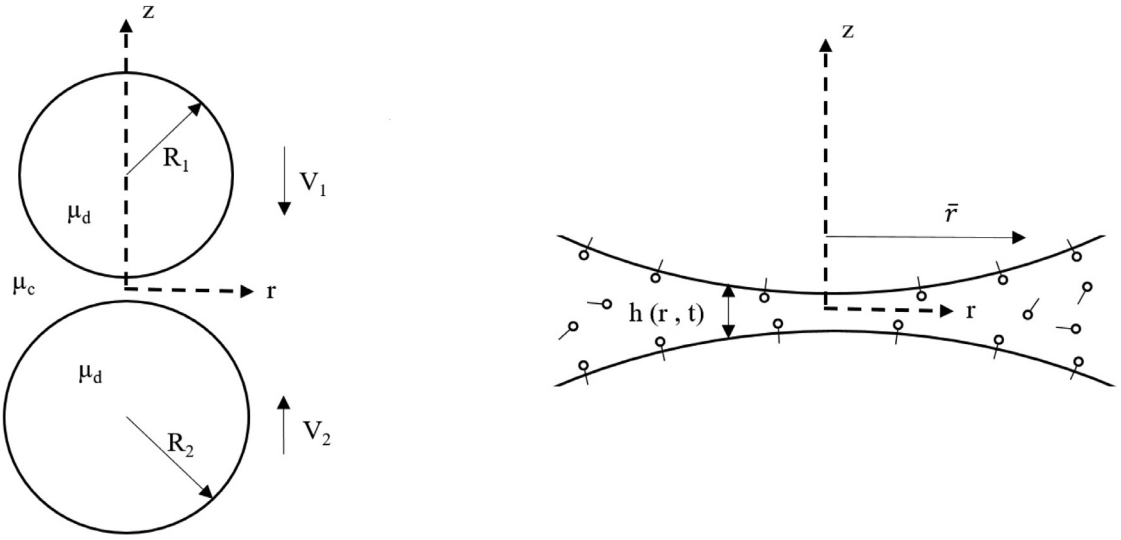

Fig. 1. Physical system depicting two fluid particles approaching each other at a constant relative velocity, and the thin film entrapped between them. The interfaces are deformable and viscous. The surfactants in the system are either confined to the interface or soluble in the continuous phase.

described by choosing r and θ as the surface coordinates. Then, by using the position vector on the surface, $\mathbf{r} = r\mathbf{e}_r + \frac{h(r,t)}{2}\mathbf{e}_z$, the tangent and the normal unit vectors are found as

$$\mathbf{t}_1 = \frac{\frac{\partial \mathbf{r}}{\partial r}}{\left|\frac{\partial \mathbf{r}}{\partial r}\right|} = \frac{\mathbf{e}_r + \frac{1}{2}\frac{\partial h}{\partial r}\mathbf{e}_z}{\sqrt{1+\frac{1}{4}\left(\frac{\partial h}{\partial r}\right)^2}}, \qquad \mathbf{t}_2 = \frac{\frac{\partial \mathbf{r}}{\partial \theta}}{\left|\frac{\partial \mathbf{r}}{\partial \theta}\right|} = \mathbf{e}_\theta,$$

$$n^{(c,d)} = \mathbf{t}_1 \times \mathbf{t}_2 = \frac{\mathbf{e}_z - \frac{1}{2}\frac{\partial h}{\partial r}\mathbf{e}_r}{\sqrt{1+\frac{1}{4}\left(\frac{\partial h}{\partial r}\right)^2}} \tag{4}$$

respectively. Here, the superscript (c, d) indicates that the unit normal vector, $\mathbf{n}^{(c,d)}$, is directed from the continuous phase to the dispersed phase. The surface gradient operator, $\nabla_\mathbf{s}$, and the surface identity tensor, $\mathtt{I}_\mathtt{s}$, can be written as

$$\nabla_\mathbf{s} = \frac{\mathbf{t}_1}{\sqrt{1+\frac{1}{4}\left(\frac{\partial h}{\partial r}\right)^2}}\frac{\partial}{\partial r} + \frac{\mathbf{t}_2}{r}\frac{\partial}{\partial \theta}, \qquad \mathtt{I}_\mathtt{s} = \mathbf{t}_1\mathbf{t}_1 + \mathbf{t}_2\mathbf{t}_2 \tag{5}$$

2.1. Governing equations and boundary conditions at the interface

The continuous phase flow is governed by the Navier–Stokes and the continuity equations

$$\rho_c\left(\frac{\partial \mathbf{v}_c}{\partial t} + \mathbf{v}_c \cdot \nabla \mathbf{v}_c\right) = -\nabla P_c + \mu_c \nabla^2 \mathbf{v}_c \tag{6}$$

$$\nabla \cdot \mathbf{v}_c = 0 \tag{7}$$

and the dispersed phase is approximated by the incompressible Stokes equations

$$\mu_d \nabla^2 \mathbf{v}_d = \nabla P_d \tag{8}$$

$$\nabla \cdot \mathbf{v}_c = 0 \tag{9}$$

where ρ, μ, $\mathbf{v}$ and P stand for the density, the viscosity, the velocity field and the pressure, respectively. The subscripts c and d denote the continuous and the dispersed phases. At the interface, the kinematic and the no-slip conditions give

$$\mathbf{v}_c|_{z=h/2} \cdot \mathbf{n}^{(c,d)} = \mathbf{u} \cdot \mathbf{n}^{(c,d)} \tag{10}$$

and

$$\mathbf{v}_c|_{z=h/2} \cdot \mathbf{t}_1 = \mathbf{u} \cdot \mathbf{t}_1 \tag{11}$$

where $\mathbf{u} = U_n\,\mathbf{n}^{(c,d)} + U\,\mathbf{t}_1$ is the interface velocity. Following Appendix C of Johns and Narayanan (2007), the normal speed of a surface can be written in terms of its implicit form, where $f(\mathbf{r}, t) = 0$ describes the surface. As the surface is given by $z = h(r, t)/2$ in this work, $f(\mathbf{r}, t)$ corresponds to $f = z - \frac{h(r,t)}{2}$. Thus, the normal component of the interfacial velocity becomes

$$U_n = -\frac{\frac{\partial f}{\partial t}}{|\nabla f|} = \frac{\frac{1}{2}\frac{\partial h}{\partial t}}{\sqrt{1+\frac{1}{4}\left(\frac{\partial h}{\partial r}\right)^2}} \tag{12}$$

and its tangential component, U, is obtained by employing the boundary integral form of the Stokes flow (reader may refer to Davis et al., 1989; Pozrikidis, 1992, and Ladyzhenskaya, 1969 for further information on the method.)

$$U = \frac{1}{\mu_d}\int_0^{r_\infty} \phi(r', \theta)\,\tau_d\,dr' \tag{13}$$

$$\phi(r', \theta) = \frac{r'}{2\pi}\int_0^{\pi} \frac{cos\,\theta}{\sqrt{r^2 + (r')^2 - 2rr'cos\,\theta}}\,d\theta \tag{14}$$

where τ_d is the tangential component of the particle side stress, i.e., $\tau_d = -\left(\mathtt{T}_\mathtt{d}|_{z=h/2} \cdot \mathbf{n}^{(c,d)}\right) \cdot \mathbf{t}_1$. The stress balance across the interface reads

$$\nabla_s \cdot \mathtt{T}_\mathtt{I} = \left[\mathtt{T}_\mathtt{c}|_{z=h/2} - \mathtt{T}_\mathtt{d}|_{z=h/2}\right] \cdot \mathbf{n}^{(c,d)} \tag{15}$$

where, $\mathtt{T}_\mathtt{c} = -P_c\mathtt{I} + \mu_c\left[\nabla \mathbf{v}_c + (\nabla \mathbf{v}_c)^\intercal\right]$ and $\mathtt{T}_\mathtt{d} = -P_d\mathtt{I} + \mu_d\left[\nabla \mathbf{v}_d + (\nabla \mathbf{v}_d)^\intercal\right]$ are the bulk stress tensors, and $\mathtt{T}_\mathtt{I}$ is the interfacial stress tensor. Following Edwards et al. (1991)'s Eq. (4.A-1) $\mathtt{T}_\mathtt{I}$ for an interface exhibiting Newtonian behavior can be written as

$$\mathtt{T}_\mathtt{I} = \mathtt{I}_\mathtt{s}[\sigma + (\kappa_I - \mu_I)\nabla_\mathbf{s} \cdot \mathbf{u}] + \mu_I\left[\nabla_\mathbf{s}\mathbf{u} \cdot \mathtt{I}_\mathtt{s} + \mathtt{I}_\mathtt{s} \cdot (\nabla_\mathbf{s}\mathbf{u})^\intercal\right] \tag{16}$$

The dilatational and the shear surface viscosities, κ_I and μ_I, and the interfacial tension, σ, are functions of the surfactant concentration at the interface. The surfactant is only allowed to be soluble in the continuous phase and its distribution inside the film is governed by

$$\frac{\partial c_c}{\partial t} + \mathbf{v}_c \cdot \nabla c_c = -\nabla \cdot \mathbf{J}_c \tag{17}$$

and the concentration balance across the interface yields

$$\frac{\partial \Gamma}{\partial t} + \nabla_\mathbf{s} \cdot (\Gamma \mathbf{u}) + \nabla_\mathbf{s} \cdot (\mathbf{J}_I \cdot \mathtt{I}_\mathtt{s}) = \mathbf{J}_c|_{z=h/2} \cdot \mathbf{n}^{(c,d)} \tag{18}$$

where, c_c and Γ are the surfactant concentration inside the film and surface excess concentration, respectively. The concentration flux $\mathbf{J_c}$ and its interfacial counterpart $\mathbf{J}_I$ are approximated by Fick's law as $\mathbf{J_c} = -D_c \nabla c_c$ and $\mathbf{J}_I = -D_I \nabla_{\mathbf{s}} \Gamma$. Here, D_I and D_c stand for the interfacial and the continuous phase diffusivity of the surfactant, respectively.

2.2. Dimensionless equations

The following transformations are applied to the Eqs. (6)–(7) and (10)–(18) to render them dimensionless

$$\tilde{h} = \frac{h}{\epsilon^2 R_p}, \quad \tilde{r} = \frac{r}{\epsilon R_p}, \quad \tilde{\sigma} = \frac{\sigma}{\sigma_0}, \quad \tilde{v_r} = \frac{v_r \mu_d}{\epsilon^2 \sigma_0}, \quad \tilde{U} = \frac{U \mu_d}{\epsilon^2 \sigma_0},$$
$$\tilde{v_z} = \frac{v_z \mu_d}{\epsilon^3 \sigma_0}, \quad \tilde{V}_{app} = \frac{V_{app}\, \mu_d}{\epsilon^3 \sigma_0}$$
$$\tilde{t} = \frac{t \epsilon \sigma_0}{\mu_d R_p}, \quad \tilde{\kappa}_I = \frac{\kappa_I}{\epsilon \mu_d R_p}, \quad \tilde{\mu}_I = \frac{\mu_I}{\epsilon \mu_d R_p}, \quad \tilde{p} = \frac{p R_p}{\sigma_0},$$
$$\tilde{\tau_d} = \frac{\tau_d R_p}{\epsilon \sigma_0}, \quad \tilde{\Gamma} = \frac{\Gamma}{\Gamma_m}, \quad \tilde{c_c} = \frac{c_c R_p}{\Gamma_m} \tag{19}$$

where, v_r and v_z are the r and z components of $\mathbf{v}_c$, p is the film side excess pressure, Γ_m is the surface excess concentration when the critical micelle concentration is reached, and σ_0 is the initial value of the interfacial tension. In the next step, the dominant terms in each transformed equation are determined based on the lubrication theory, as the small parameter $\epsilon << 1$. Then, the simplified versions of Eqs. (6)–(7) and (10)–(11) in the dimensionless form give

$$\lambda^* \frac{\partial \tilde{p}}{\partial \tilde{r}} = \frac{\partial^2 \tilde{v_r}}{\partial \tilde{z}^2}, \qquad \frac{\partial \tilde{p}}{\partial \tilde{z}} = 0 \tag{20}$$

$$\frac{\partial \tilde{v_z}}{\partial \tilde{z}} + \frac{1}{\tilde{r}} \frac{\partial}{\partial \tilde{r}} (\tilde{r} \tilde{v_r}) = 0 \tag{21}$$

$$\frac{1}{2} \frac{\partial \tilde{h}}{\partial \tilde{t}} = \tilde{v_z}|_{\tilde{z}=\tilde{h}/2} - \frac{1}{2} \frac{\partial \tilde{h}}{\partial r} \tilde{v_r}|_{\tilde{z}=\tilde{h}/2} \tag{22}$$

$$\tilde{v_r}|_{\tilde{z}=\tilde{h}/2} = \tilde{U} \tag{23}$$

where $\lambda^* = \frac{\epsilon \mu_d}{\mu_c}$. The normal and the tangential components of the stress balance, Eq. (15), become

$$\tilde{p} = 2 - \frac{1}{2\tilde{r}} \frac{\partial}{\partial \tilde{r}} \left(\tilde{r} \frac{\partial \tilde{h}}{\partial \tilde{r}} \right) + \frac{A^*}{\tilde{h}^3} \tag{24}$$

and

$$\frac{\partial}{\partial \tilde{r}} \left[(\tilde{\kappa}_I + \tilde{\mu}_I) \frac{1}{\tilde{r}} \frac{\partial}{\partial \tilde{r}} (\tilde{r} \tilde{U}) \right] + \frac{\partial \tilde{\sigma}'}{\partial \tilde{r}} - 2 \frac{\partial \tilde{\mu}_I}{\partial \tilde{r}} \frac{\tilde{U}}{\tilde{r}} = \frac{1}{\lambda^*} \frac{\partial \tilde{v_r}}{\partial \tilde{z}} \bigg|_{\tilde{z}=\tilde{h}/2} + \tilde{\tau_d} \tag{25}$$

respectively. In the normal component of the stress balance, the deviations in the particle side pressure is neglected and the non-dimensionalized Hamaker constant, $A^* = \frac{A}{6\pi\epsilon^6 R_p^2 \sigma_0}$, represents the effect of the attractive van der Waals forces. In the tangential component, τ_I is determined via Eq. (16), and $\tilde{\sigma}' = \frac{1}{\epsilon^2}\tilde{\sigma}$. The surface excess concentration is taken as uniformly distributed initially, and the initial condition is given by $\tilde{\Gamma}(\tilde{r}, 0) = \Gamma_0$. As relatively low surface excess concentration values are examined in this work, the surface viscosities are assumed to be linear functions of $\tilde{\Gamma}$ and described using the initial condition Γ_0 as:

$$\tilde{\kappa}_I = Bo_\kappa \frac{\tilde{\Gamma}}{\Gamma_0}, \qquad \tilde{\mu}_I = Bo_\mu \frac{\tilde{\Gamma}}{\Gamma_0} \tag{26}$$

where the dilatational and the shear Boussinesq numbers are defined via the initial values of the surface viscosities, $\tilde{\kappa}_{I0}$ and $\tilde{\mu}_{I0}$, as $Bo_\kappa = \tilde{\kappa}_{I0} = \frac{\kappa_{I0}}{\epsilon \mu_d R_p}$ and $Bo_\mu = \tilde{\mu}_{I0} = \frac{\mu_{I0}}{\epsilon \mu_d R_p}$. The surface tension gradient is expressed as

$$\frac{\partial \tilde{\sigma}'}{\partial \tilde{r}} = \tilde{\sigma}'_{\tilde{\Gamma}} \frac{\partial \tilde{\Gamma}}{\partial \tilde{r}} \tag{27}$$

where $\tilde{\sigma}'_{\tilde{\Gamma}} = \frac{\Delta \tilde{\sigma}}{\Delta \tilde{\Gamma}} \frac{1}{\epsilon^2}$, and an estimation on its magnitude is given in Appendix A. Then, the tangential stress balance, Eq. (25), can be written as

$$Bo \frac{\partial}{\partial \tilde{r}} \left[\frac{\tilde{\Gamma}}{\Gamma_0} \frac{1}{\tilde{r}} \frac{\partial}{\partial \tilde{r}} (\tilde{r} \tilde{U}) \right] + \tilde{\sigma}'_{\tilde{\Gamma}} \frac{\partial \tilde{\Gamma}}{\partial \tilde{r}} - 2 Bo_\mu \frac{\partial}{\partial \tilde{r}} \left(\frac{\tilde{\Gamma}}{\Gamma_0} \right) \frac{\tilde{U}}{\tilde{r}} = \frac{1}{\lambda^*} \frac{\partial \tilde{v_r}}{\partial \tilde{z}} \bigg|_{\tilde{z}=\tilde{h}/2} + \tilde{\tau_d} \tag{28}$$

Here, $Bo = Bo_\kappa + Bo_\mu$ is the Boussinesq number. The boundary integral equations, Eqs. (13) and (14), become

$$\tilde{U} = \int_0^{\tilde{r}_\infty} \tilde{\phi}(\tilde{r}', \theta) \tilde{\tau}_d \, d\tilde{r}' \tag{29}$$

and

$$\tilde{\phi}(\tilde{r}', \theta) = \frac{\tilde{r}'}{2\pi} \int_0^\pi \frac{\cos\theta}{\sqrt{\tilde{r}^2 + (\tilde{r}')^2 - 2\tilde{r}\tilde{r}'\cos\theta}} \, d\theta \tag{30}$$

Notice that, the transformation of r also applies to the integration variable r'. The governing equation for the concentration inside the film, Eq. (17) reduces to

$$\epsilon^2 Pe \left(\frac{\partial \tilde{c_c}}{\partial \tilde{t}} + \tilde{v_r} \frac{\partial \tilde{c_c}}{\partial \tilde{r}} + \tilde{v_z} \frac{\partial \tilde{c_c}}{\partial \tilde{z}} \right) = \frac{\partial^2 \tilde{c_c}}{\partial \tilde{z}^2} \tag{31}$$

where the Péclet number is defined as $Pe = \epsilon^3 \frac{R_p \sigma_0}{D_c \mu_d}$. Eq. (31) indicates that its left hand side is negligible unless $\frac{R_p \sigma_0}{D_c \mu_d}$ is on the order of ϵ^{-5} or greater, which is shown to be unlikely in Appendix A. Then, by neglecting the left hand side, the concentration equation can be written as

$$0 \approx \frac{\partial^2 \tilde{c_c}}{\partial \tilde{z}^2} \tag{32}$$

indicating that $\tilde{c_c}$ is a linear function of $\tilde{z}$. Also, due to the symmetry around the r axis, $\frac{\partial \tilde{c_c}}{\partial \tilde{z}}\big|_{\tilde{z}=0}$ should be zero, meaning that $\tilde{c_c}$ is actually constant within the film. The concentration balance across the interface, Eq. (18), gives

$$Pe_s \left[\frac{\partial \tilde{\Gamma}}{\partial \tilde{t}} + \frac{1}{\tilde{r}} \frac{\partial}{\partial \tilde{r}} (\tilde{r} \tilde{\Gamma} \tilde{U}) \right] - \frac{1}{\tilde{r}} \frac{\partial}{\partial \tilde{r}} \left(\tilde{r} \frac{\partial \tilde{\Gamma}}{\partial \tilde{r}} \right) = 0 \tag{33}$$

Notice that the right hand side of the equation appears to be zero since $\tilde{c_c}$ is constant throughout the film, and consequently the surfactant is confined to the interface. Therefore, the analyses carried out via Eq. (33) should be valid for both insoluble surfactants and for the ones that are only soluble in the continuous phase. The surface counterpart of the Péclet number is defined as $Pe_s = \epsilon^3 \frac{R_p \sigma_0}{D_I \mu_d}$. Although the surface Péclet number has a factor of ϵ^3 in it, for the typical systems of interest, it is not always small enough to render the convective terms in Eq. (33) negligible. In Appendix A, the estimates for Pe_s for systems of 1 mm fluid particles in water with different viscosity ratios are found as: between $Pe_s \approx 200$ and $Pe_s \approx 2000$ for bubbles in water ($\mu_d/\mu_c << 1$), in the range of $Pe_s \approx 2.5$ to $Pe_s \approx 25$ for droplets with comparable viscosity ($\mu_d \approx \mu_c$), and $Pe_s << 0.25$ for highly viscous droplets ($\mu_d >> \mu_c$). The estimated values imply that the convective terms are only negligible for the droplets with high viscosity. Therefore, when μ_d is not significantly larger than μ_c, the concentration jump condition is used as presented in Eq. (33). When $\mu_d >> \mu_c$, on the other hand, it simplifies to

$$\frac{1}{\tilde{r}} \frac{\partial}{\partial \tilde{r}} \left(\tilde{r} \frac{\partial \tilde{\Gamma}}{\partial \tilde{r}} \right) = 0 \tag{34}$$

in the low Pe_s limit. Eq. (34) has a solution in the form of $\tilde{\Gamma} = K_1 \ln(\tilde{r}) + K_2$, where K_1 and K_2 are integration constants. Since $\tilde{\Gamma}$ has to be finite at the center of axisymmetry, i.e., at $\tilde{r} = 0$, K_1 must be zero. Then, $\tilde{\Gamma}$ attains a constant value, i.e., $\tilde{\Gamma}(\tilde{r}, \tilde{t}) = \Gamma_0$, and as a result the interfacial properties, $\tilde{\kappa}_I$, $\tilde{\mu}_I$ and $\tilde{\sigma}'$ are also constants throughout the interface.

Hereafter, tildes in the dimensionless variables are omitted. Solution of Eq. (20) subjected to the no-slip condition, Eq. (23), together with the symmetry condition around r axis, gives

$$v_r = \frac{\lambda^*}{2}\frac{\partial p}{\partial r}\left(z^2 - \left(\frac{h}{2}\right)^2\right) + U \tag{35}$$

The z component of the velocity, then, can be determined via Eq. (21). By substituting v_r and v_z into the kinematic condition, Eq. (22), the thinning equation is found as:

$$\frac{\partial h}{\partial t} = \frac{1}{r}\left[\frac{\lambda^*}{12}\frac{\partial}{\partial r}\left(r\frac{\partial p}{\partial r}h^3\right) - \frac{\partial}{\partial r}(rUh)\right] \tag{36}$$

By inserting v_r from Eqs. (35), (28) is rewritten as

$$Bo\frac{\partial}{\partial r}\left[\frac{\Gamma}{\Gamma_0}\frac{1}{r}\frac{\partial}{\partial r}(rU)\right] + \sigma'_\Gamma\frac{\partial \Gamma}{\partial r} - 2Bo_\mu\frac{\partial}{\partial r}\left(\frac{\Gamma}{\Gamma_0}\right)\frac{U}{r} - \frac{h}{2}\frac{\partial p}{\partial r} = \tau_d \tag{37}$$

Then, the boundary integral equation, Eq. (29), is rewritten by substituting τ_d through Eq. (37)

$$U = \int_0^{r_\infty} \phi(r', \theta)\left\{Bo\frac{\partial}{\partial r}\left[\frac{\Gamma}{\Gamma_0}\frac{1}{r}\frac{\partial}{\partial r}(rU)\right] + \sigma'_\Gamma\frac{\partial \Gamma}{\partial r} - 2Bo_\mu\frac{\partial}{\partial r}\left(\frac{\Gamma}{\Gamma_0}\right)\frac{U}{r} - \frac{h}{2}\frac{\partial p}{\partial r}\right\} dr' \tag{38}$$

In the case of uniform Γ distribution, where $\Gamma(r, t) = \Gamma_0$, Eqs. (37) and (38) simplify into

$$Bo\frac{\partial}{\partial r}\left[\frac{1}{r}\frac{\partial}{\partial r}(rU)\right] - \frac{h}{2}\frac{\partial p}{\partial r} = \tau_d \tag{39}$$

and

$$U = \int_0^{r_\infty} \phi(r', \theta)\left\{Bo\frac{\partial}{\partial r}\left[\frac{1}{r}\frac{\partial}{\partial r}(rU)\right] - \frac{h}{2}\frac{\partial p}{\partial r}\right\} dr' \tag{40}$$

which can be used for the high viscosity droplets ($\mu_d >> \mu_c$) case. The axsymmetric nature of the problem requires

$$\left.\frac{\partial p}{\partial r}\right|_{r=0} = 0, \qquad \left.\frac{\partial h}{\partial r}\right|_{r=0} = 0, \qquad U|_{r=0} = 0, \qquad \left.\frac{\partial \Gamma}{\partial r}\right|_{r=0} = 0 \tag{41}$$

and it is assumed that at a large enough radial distance, at $r = r_\infty$, the collision does not affect the local shape of the interface, V_{app}, U or Γ

$$p|_{r=r_\infty} = 0, \qquad \left.\frac{\partial h}{\partial t}\right|_{r=r_\infty} = -V_{app}, \qquad \left.\frac{\partial U}{\partial r}\right|_{r=r_\infty} = 0, \qquad \left.\frac{\partial \Gamma}{\partial r}\right|_{r=r_\infty} = 0 \tag{42}$$

In addition, the axisymmetry also implies $\tau_d = 0$ at $r = 0$. By substituting this condition together with the symmetry conditions in Eq. (41) into the tangential stress balance, Eq. (37) or Eq. (39), an additional constraint that has to be satisfied by U emerges:

$$\left\{\frac{\partial}{\partial r}\left[\frac{1}{r}\frac{\partial}{\partial r}(rU)\right]\right\}\Bigg|_{r=0} = 0 \tag{43}$$

Finally, the initial condition, $h(r, 0)$, is taken as

$$h(r, 0) = 2 + r^2 \tag{44}$$

to resemble the shape of a perfect sphere initially.

3. Numerical procedure

The problem requires the solution of Eqs. (24), (33), (36), and (38), where the boundary conditions Eqs. (41) and (42) hold together with the constraint given by Eq. (43). In the limit of small Pe_s, on the other hand, Eq. (33) is not solved as Γ is uniform throughout the interface, and Eq. (40) is employed instead of Eq. (38). The spatial derivatives are discretized via a spectral scheme based on the Chebyshev polynomials as described in Chapter 6 of Trefethen (2000), whereas the second order backward differentiation is employed for the time derivatives. As can be seen from Eq. (30), the boundary integral equation kernel, ϕ, has a singularity of mathematical origin, appearing when $r = r'$ and $\theta = 0$. To treat this singularity, Ozan and Jakobsen (2019) is followed and the integration in Eq. (38) (or in Eq. (40)) is written in matrix form as

$$U = [A]\tau_d = [A]\left\{Bo\frac{\partial}{\partial r}\left[\frac{\Gamma}{\Gamma_0}\frac{1}{r}\frac{\partial}{\partial r}(rU)\right] + \sigma'_\Gamma\frac{\partial \Gamma}{\partial r} - 2Bo_\mu\frac{\partial}{\partial r}\left(\frac{\Gamma}{\Gamma_0}\right)\frac{U}{r} - \frac{h}{2}\frac{\partial p}{\partial r}\right\} \tag{45}$$

or as

$$U = [A]\left\{Bo\frac{\partial}{\partial r}\left[\frac{1}{r}\frac{\partial}{\partial r}(rU)\right] - \frac{h}{2}\frac{\partial p}{\partial r}\right\} \tag{46}$$

The details for the purely geometric integration matrix $[A]$ is provided in the Appendix of Ozan and Jakobsen (2019).

4. Results and discussion

The results presented in this work are divided into three groups: In Section 4.1, coalescence of the particles is not taken into consideration by neglecting the attractive Van der Waals forces ($A^* = 0$), to investigate the effect of the surface viscosities on the film drainage process and the tangential velocity of the interface. Then, the coalescence behavior (e.g. the coalescence time and the type of rupture) in the presence of the surface viscosities is examined for the droplets with high viscosity in the low Pe_s limit in Section 4.2, and for the fluid particles whose viscosity is comparable to/lower than that of the continuous phase, in Section 4.3. In Section 4.2, as Pe_s is low, the surface excess concentration is uniformly distributed throughout the interface. On the other hand, in Section 4.3, the distribution is non-uniform and governed by Eq. (33). The non-uniform distribution of the surface excess concentration also results in surface tension gradient driven flows along the interface. This allows a comparison between the effects of different surface related mechanisms, i.e., the surface viscosities and the surface tension driven flow. The model employed in this work is an extension of the model proposed by Ozan and Jakobsen (2019) to contaminated interfaces. Therefore, in the absence of the surfactants, the current model is capable of reproducing their results, as well as the results of Bazhlekov et al. (2000) and Klaseboer et al. (2000) as shown in Figs. 3 and 6 of Ozan and Jakobsen (2019).

4.1. Drainage without attractive van der Waals forces

In this section, the effect of the surface viscosities, κ_I and μ_I, on the drainage and the mobility of the interface is examined. The magnitude of κ_I and μ_I are manipulated through the Boussinesq number, Bo, and the other parameters are kept constant. The viscosity ratio and the approach velocity are selected as $\lambda^* = 10$ and $V_{app} = 1$, respectively. Since the viscosity ratio is large, the results are obtained in the low Pe_s limit where Γ is uniformly distributed. The non-dimensionalized Hamaker constant,

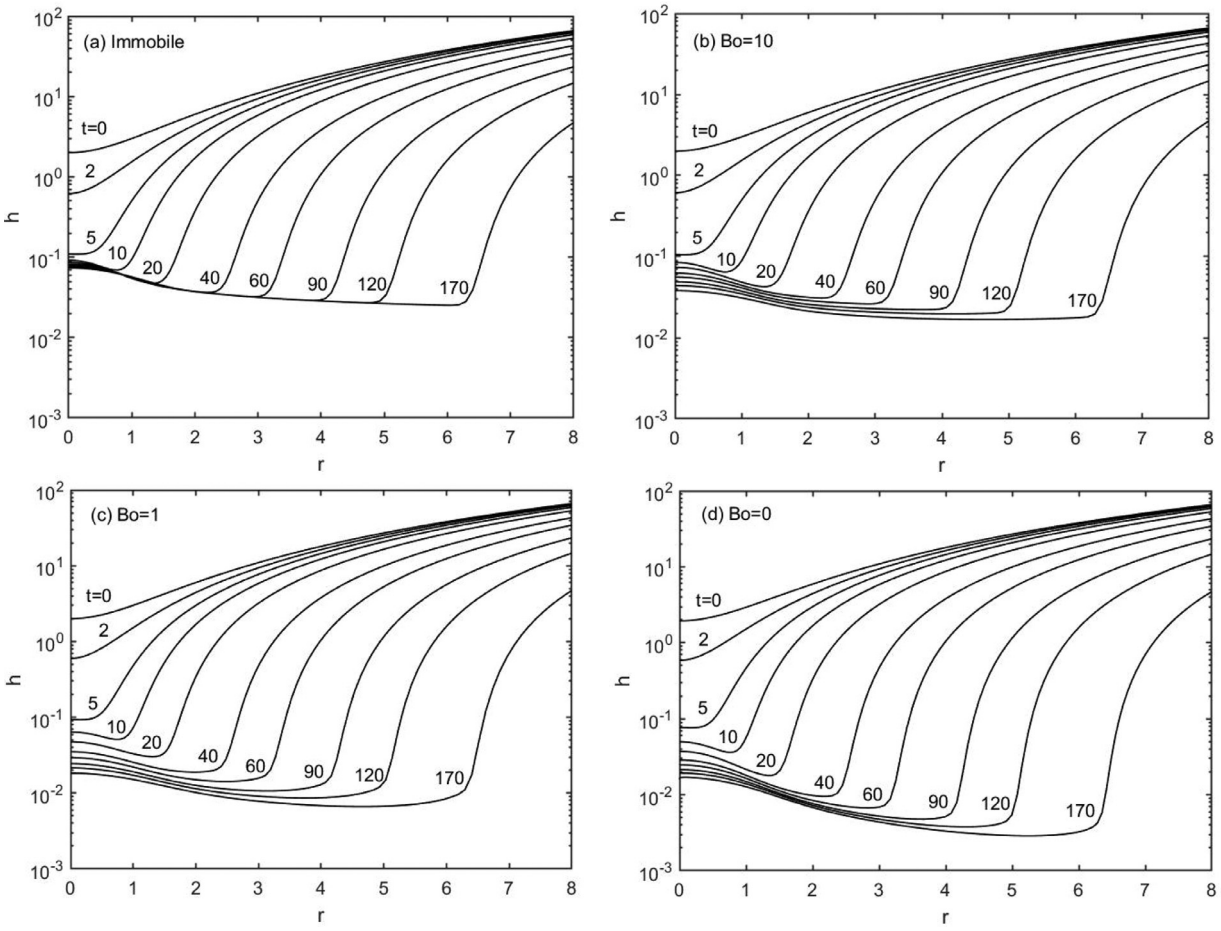

Fig. 2. Time evolution of the film thickness profile (a) for an immobile interface, (b) for $Bo = 10$, (c) for $Bo = 1$ and (d) for an inviscid interface ($Bo = 0$). All profiles are obtained with $\lambda^* = 10$, $A^* = 0$ and $r_\infty = 30$.

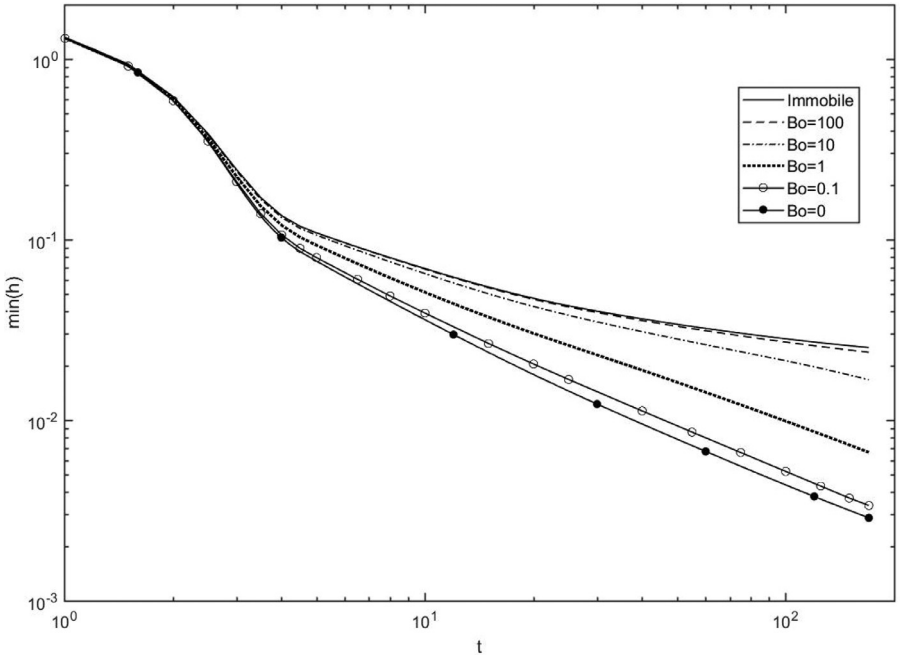

Fig. 3. The minimum film thickness as a function of time for different values of *Bo*. All results are obtained with $\lambda^* = 10$, $A^* = 0$ and $r_\infty = 30$.

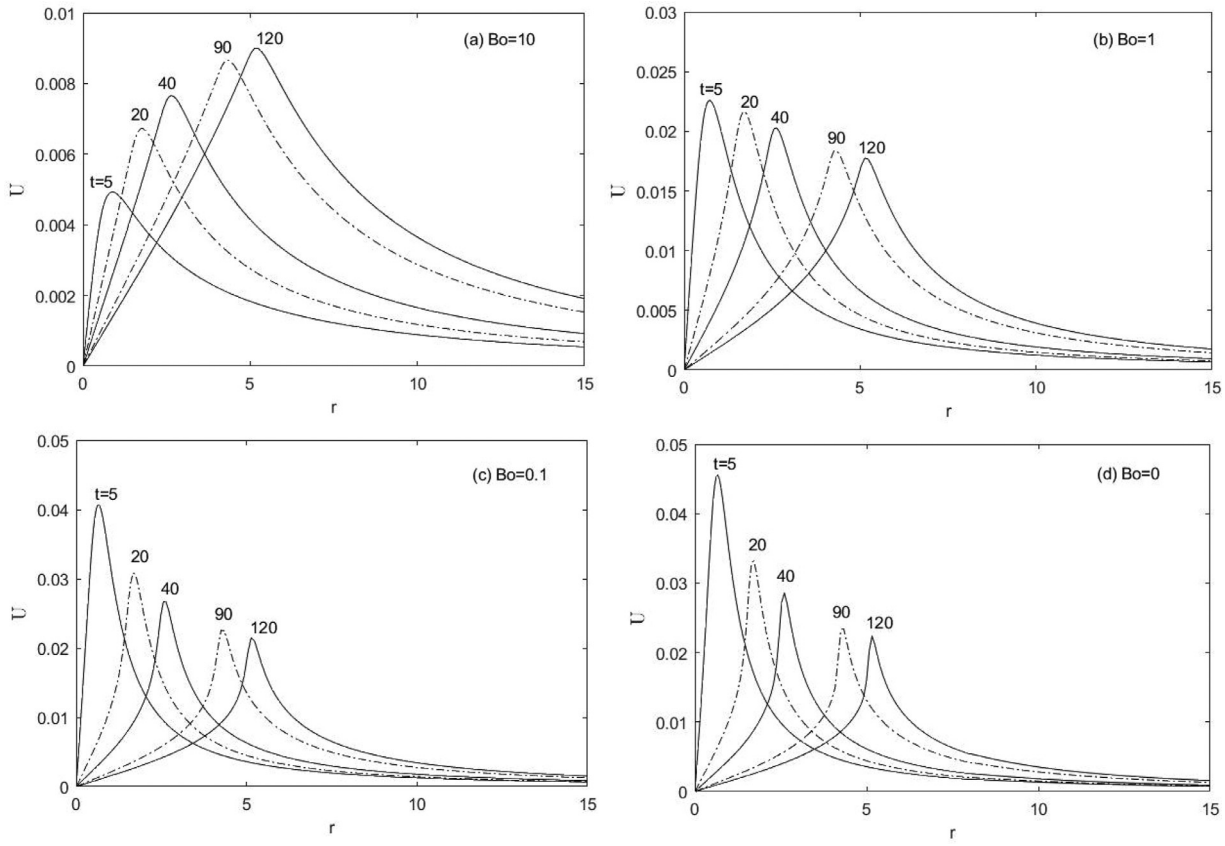

Fig. 4. Time evolution of the tangential velocity of the interface (a) for $Bo = 10$, (b) for $Bo = 1$, (c) for $Bo = 0.1$ and (d) for an inviscid interface ($Bo = 0$). All profiles are obtained with $\lambda^* = 10$, $A^* = 0$ and $r_\infty = 30$.

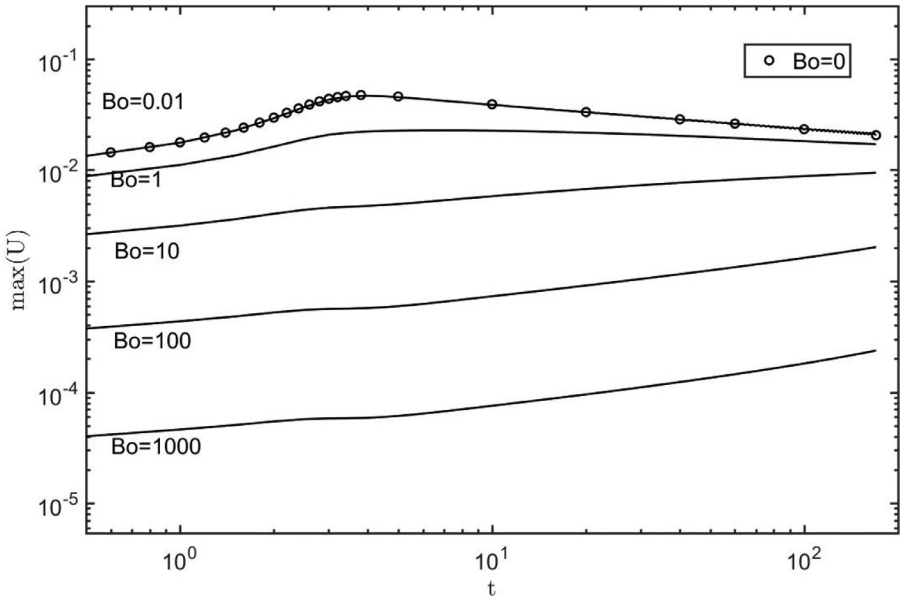

Fig. 5. The maximum value of the tangential velocity of the interface as a function of time for different values of Bo. All results are obtained with $\lambda^* = 10$, $A^* = 0$ and $r_\infty = 30$.

A^*, is taken as zero, and consequently the rupture of the interface is not considered. Figs. 2 and 3 present the time evolution of $h(r, t)$, and the minimum film thickness as a function of time, respectively, for different values of Bo. The time evolution of $h(r, t)$ and the minimum thickness curve for $\lambda^* = 10$ and $Bo = 0$, given in Figs. 2(d) and 3 respectively, are in perfect visual agreement with Bazhlekov et al. (2000)'s results for $\lambda^* = 10$ (their Figs. 4(b) and 5), where the surface viscosities are not considered in the drainage model. The results for the immobile interface case are obtained by neglecting the second term on the right hand side of Eq. (36).

Fig. 3 shows that as Bo increases, i.e., the interface becomes more viscous, the drainage behavior approaches to that of the immobile interface's. This implies that even when the surface excess concentration is uniformly distributed, i.e., in the absence of sur-

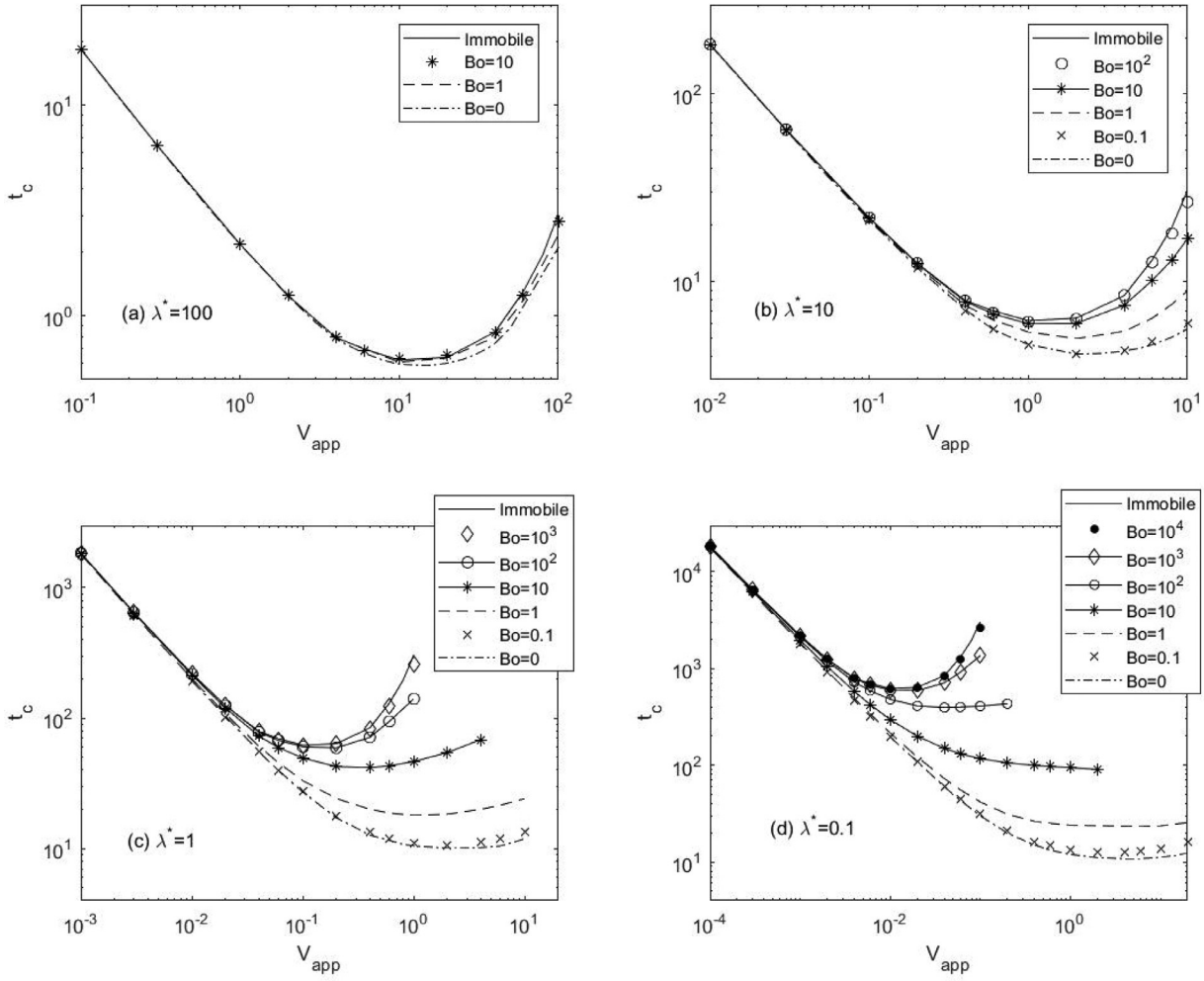

Fig. 6. Coalesence time as a function of the approach velocity and *Bo* for (a) $\lambda^* = 100$, (b) $\lambda^* = 10$, (c) $\lambda^* = 1$ and (d) $\lambda^* = 0.1$. All results are obtained with $A^* = 10^{-3}$ and $r_\infty = 30$.

face tension gradients, the immobilization of the interface is still possible due to surface viscosities. The minimum film thickness at a given time is observed to be higher for more viscous interfaces, showing that the drainage rate is slower for higher values of *Bo*. This can be explained through Eq. (36). Since the surface viscosities, κ_I and μ_I, denote the resistance of the interface to tangential deformations, as the value of *Bo* increases, the magnitude of U is anticipated to decrease. As a result, the last term in Eq. (36) signifying the contribution of U to the thinning of the film is smaller for more viscous interfaces, and consequently, the drainage rate is slower for them. Fig. 3 also reveals that *Bo* values as small as 0.1 may affect the drainage rate, as the minimum thickness curve corresponding to $Bo = 0.1$ is different than the one for the inviscid interface with $Bo = 0$. On the other hand, the curve for $Bo = 100$ is almost indistinguishable from the curve for the immobile interface, showing that the interface can be modeled as an immobilized one for $Bo \geq 100$ for the particular parameter set considered here. In addition, as can be seen from Fig. 2, the dimple formation is observed around the same time ($t \approx 5$) regardless of the value of *Bo*, and the radial position of the rim shifts towards larger r with time. The latter observation is expected to be seen in the constant approach velocity collisions as the interaction force between the particles increases with time (Abid and Chesters, 1994; Chan et al., 2011). However, Fig. 3 reveals that the minimum film thickness at which the dimpling starts (at $t \approx 5$), is larger for more viscous interfaces, as the drainage rate is smaller for them.

The time evolution of U for different values of *Bo* is presented in Fig. 4. Although the maximum value of U decreases drastically with increasing values of *Bo*, the radial position at which U attains its maximum value is approximately same for all *Bo* values presented. To achieve clearer visualization, the profiles in Fig. 4 are presented for $r = [0, 15]$ instead of the whole computational domain, $r = [0, 30]$. However, it should be noted that the tangential velocity not only satisfies the boundary condition given by Eq. (42) at $r = r_\infty = 30$, but also plateaus around $U \approx 0$ before r_∞ is reached, indicating that the selected value of r_∞ is indeed a large enough value and the collision has no effect on the conditions at the end of the domain.

The immobilization due to the surface viscosities can be more clearly seen via Fig. 5, where the maximum value of U is given as a function of time for different values of *Bo*. An order of magnitude increase in the values of the surface viscosities for $Bo \geq 1$ results in an order of magnitude decrease in the maximum value of the tangential velocity, and as a result U quickly becomes insignificant for the drainage process. Previously in this section, it has been concluded that the interfaces immobilize for $Bo \geq 100$. By merging this observation with Fig. 5, it can be seen that the same condition can be roughly expressed in terms of U as $\max(U) \leq 10^{-3}$. On the other hand, Fig. 5 also reveals that $\max(U)$ profiles are identical when $Bo = 0.01$ and $Bo = 0$, showing that the effect of the surface viscosities on the drainage is negligible around and below this value. Then, for the particular set of parameters investigated here,

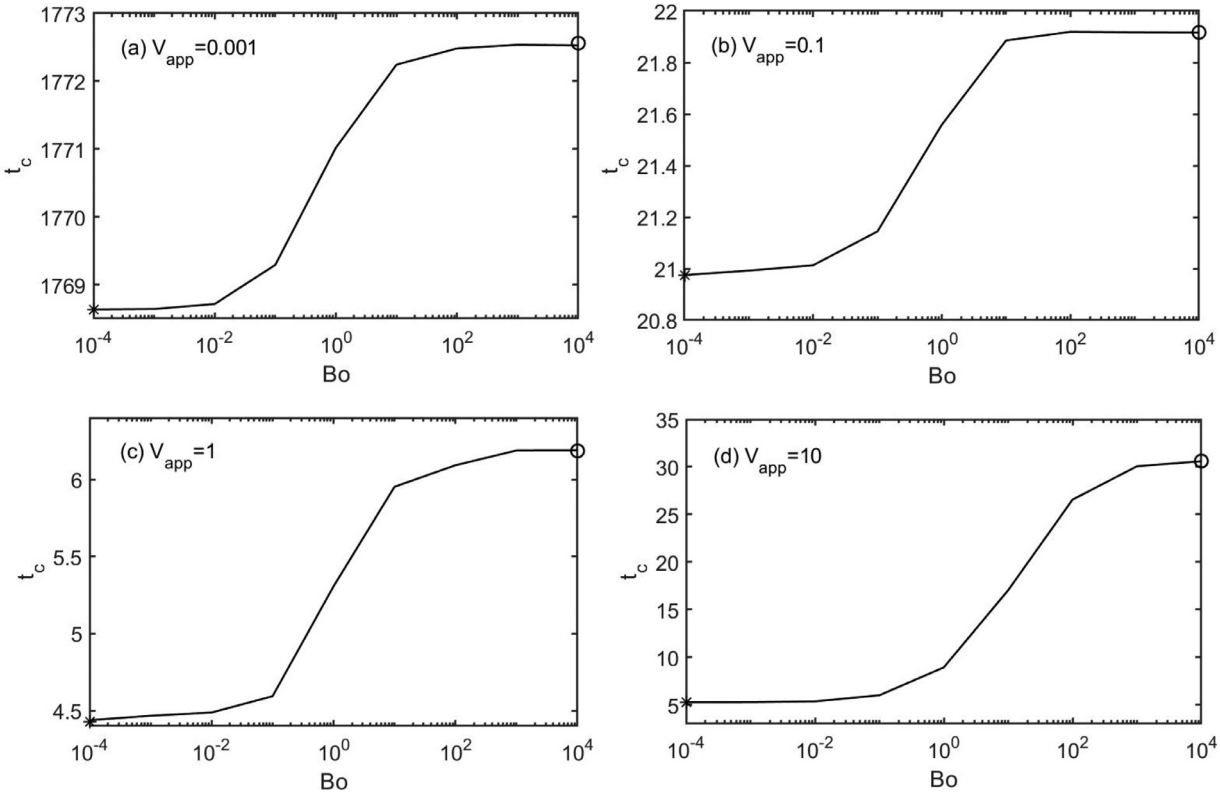

Fig. 7. Coalescence time as a function of Bo at (a) $V_{app} = 0.001$, (b) $V_{app} = 0.1$, (c) $V_{app} = 1$ and (d) $V_{app} = 10$. The asterisk and the circle mark $Bo = 0$ and immobile case results. All results are obtained with $\lambda^* = 10$, $A^* = 10^{-3}$ and $r_\infty = 30$.

a conclusion can be drawn to understand the importance of surface viscosities in the film drainage: When $Bo \geq 100$, the interface is completely immobilized, the effect of U on the drainage is negligible and consequently the drainage behavior becomes independent of the magnitude of the surface viscosities; when $Bo \leq 0.01$, the surface viscosities are not large enough to affect U significantly and therefore can be excluded from the model; when Bo is in between these limits, the surface viscosities play an important role and have to be taken into account in the drainage model.

4.2. Coalescence of high viscosity droplets

Although the rupture of the interface itself is not modeled in this work, it is possible to estimate the rupture, thus the coalescence of the particles, by taking the attractive van der Waals forces into consideration via a non-zero value of A^*. As the film drains, the attractive forces become more and more significant, and overcome the resistance within the film once the film thickness reaches a small enough value. Consequently, the film begins to drain very rapidly. This is expected to result in the rupture of the film and the coalescence of the particles. Therefore, the rapid thinning regime is accepted as the onset of the rupture/coalescence in our simulations, and the drainage time is taken as the time of coalescence, as the time scale of the rupture is typically much smaller than that of the film drainage.

Since this section focuses on the coalescence of the droplets with high viscosities, as discussed in Section 2.2, the model is once again solved in the low Pe_s limit, meaning that the surfactant distribution is uniform and Marangoni stresses are negligible. The time of coalescence, t_c, is given as a function of the relative approach velocity, V_{app}, and the Boussinesq number Bo, for $A^* = 10^{-3}$ and different values of λ^* in Fig. 6. It should be noted that the smallest λ^* value in Fig. 6, $\lambda^* = 0.1$, still corresponds to a relatively high value μ_d/μ_c as λ^* has a factor of ϵ in it (for further details on the estimation of the dimensionless parameters the reader may consult to Appendix A). The immobilizing effect of the surface viscosities that has been discussed in Section 4.1, is also revealed here as the t_c curves are closer to the immobile ones for higher values of Bo for all λ^*. From Fig. 6(a), it is seen that the t_c values for the immobile interface and the inviscid interface ($Bo = 0$) are very close to each other, meaning that roughly $\lambda^* \geq 100$ is sufficient to immobilize the interface by itself, without requiring immobilization due to surface phenomena such as the Marangoni flow or the surface viscosities. The results for $\lambda^* < 100$ show that $Bo\lambda^* \approx 1000$ is the limit after which the interface is completely immobilized. Notice that this criterion signifies the ratio of the surface viscous forces to the film side bulk viscous forces and do not change with the dispersed phase viscosity or depend on the small parameter ϵ, since $Bo\lambda^* = \frac{\kappa_{I0}+\mu_{I0}}{\epsilon\mu_d R_p}\frac{\epsilon\mu_d}{\mu_c} = \frac{\kappa_{I0}+\mu_{I0}}{\mu_c R_p}$. On the other hand, Bo values as small as 1 seem to affect t_c dramatically.

The three distinct drainage/coalescence regimes reported by Ozan and Jakobsen (2019) as V_{app} increases, are also observed here, apart from some exceptions, e.g. for $Bo = 10$ and $\lambda^* = 0.1$ in Fig. 6(d). In the first region, a linear relation between $\log(t_c)$ and $\log(V_{app})$ is observed until a critical velocity, V_{dimp}, is reached. In this linear regime, no dimples are observed and the rupture occurs at $r = 0$. When $V_{app} \geq V_{dimp}$, the interface dimples, the rupture occurs at the rim instead of $r = 0$, and the trend between $\log(t_c)$ and $\log(V_{app})$ starts to deviate from a linear one. As V_{app} is further increased, t_c passes through a minimum at another critical velocity, V_{mult}. This critical velocity marks the end of the dimpled drainage regime and once it is reached, multiple rim-like structures appear. The slope $d(\log(t_c))/d(\log(V_{app}))$ in the first regime, the critical velocities and their dependence on λ^* and A^* are discussed in detail in Ozan and Jakobsen (2019). Fig. 6 shows that Bo has little to no effect on t_c in the first region. However, the

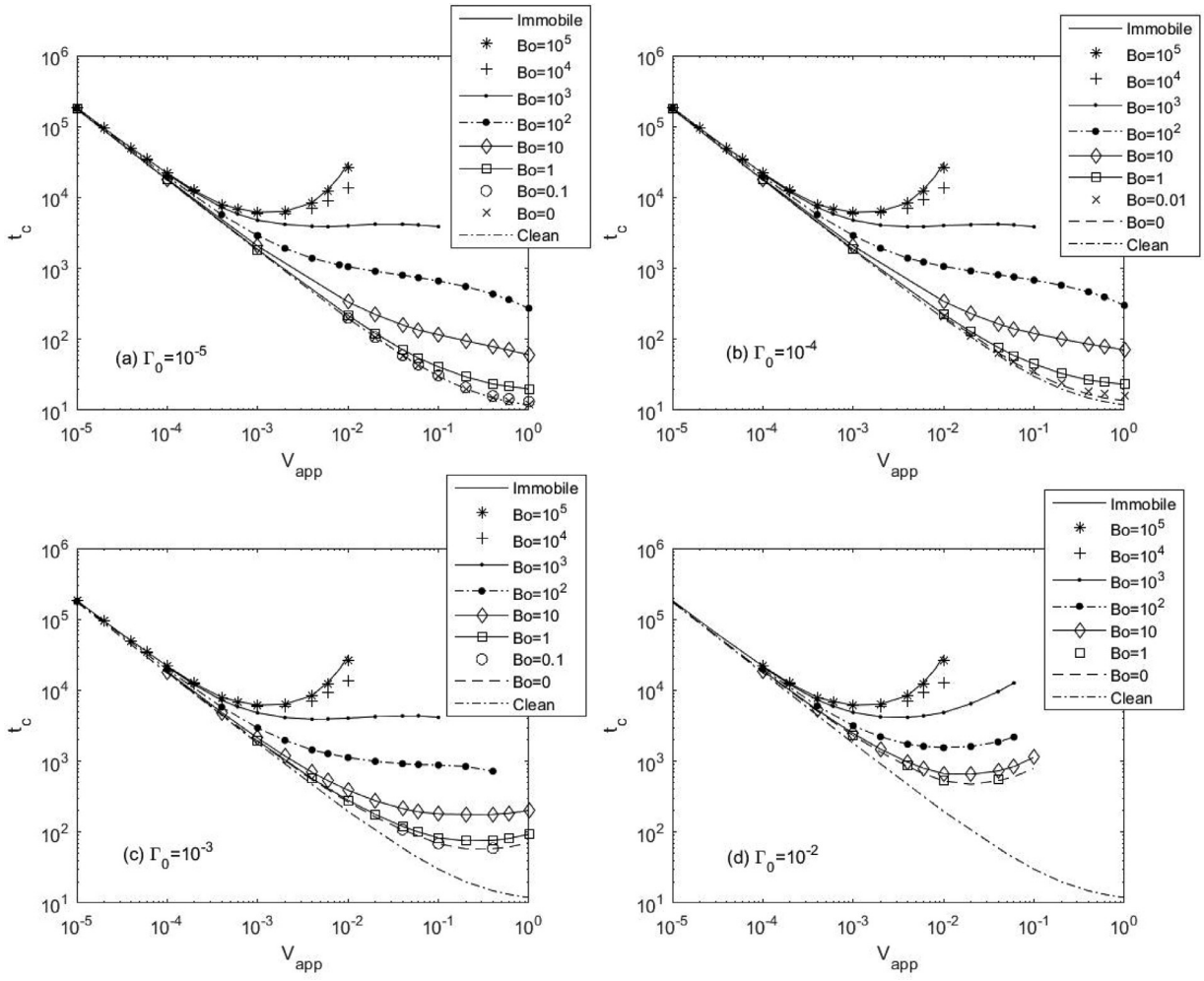

Fig. 8. Coalescence time for $\mu_d \approx \mu_c$ and $Pe_s = 2.5$ as a function of V_{app} and Bo with (a) $\Gamma_0 = 10^{-5}$, (b) $\Gamma_0 = 10^{-4}$, (c) $\Gamma_0 = 10^{-3}$ and (d) $\Gamma_0 = 10^{-2}$. All results are obtained, $A^* = 10^{-3}$ and $r_\infty = 30$.

effect is amplified as V_{app} increases, especially with the beginning of the deviations in the interface shape, i.e., after the linear regime. This behavior can be observed through Fig. 7 in a more clear way, where t_c is given as a function of Bo for $\lambda^* = 10$ at chosen values of V_{app}. These values are chosen to represent different drainage/coalescence regimes: $V_{app} = 0.001$ corresponds to linear regime for all values of Bo, at $V_{app} = 0.1$ the dimple formation is observed only for very high values of Bo, $V_{app} = 1$ falls into the dimpled drainage region for all values of Bo, and at $V_{app} = 10$ the interface has multiple rims regardless of the value of Bo. The immobilization of the interface gives only a negligible increase of ≈ 0.2 in t_c at $V_{app} = 0.001$, i.e., when the drainage falls into the linear region. However, when the dimples begin to emerge, the difference becomes non-negligible and increases drastically with V_{app}, as it is $\approx 4\%$ and $\approx 40\%$ for $V_{app} = 0.1$ and $V_{app} = 1$, respectively. When V_{app} is further increased to 10, the immobilization of the interface results in a change in the order of magnitude of t_c, as the difference is found as $\approx 500\%$. Thus, the effect of the surface viscosities on t_c is negligible only when both the immobile and the inviscid interfaces do not exhibit any dimple formation.

4.3. Coalescence of droplets with $\mu_d \approx \mu_c$ or bubbles

As shown in Appendix A, for the systems where μ_d is not much larger than μ_c, Pe_s is typically not small enough to make the convective terms in Eq. (33) negligible. Therefore, the distribution of the surface excess concentration, Γ, is governed by Eq. (33) instead of being uniform. The non-uniform distribution introduces surface gradient driven flows along the interface, i.e., Marangoni flows, as well as gradients of the surface viscosities. Furthermore, now an initial condition for the surface excess concentration is required. The initial condition, Γ_0, is chosen to be small, to represent the concentration levels that might be considered as unintentionally introduced 'impurities'. For the systems with comparable dispersed and continuous phase viscosities, other parameters are taken as $\lambda^* = 10^{-2}$ and $Pe_s = 2.5$ or $Pe_s = 25$, whereas for bubbles in liquids with viscosities comparable to that of water $\lambda^* = 10^{-4}$ and either $Pe_s = 200$ or $Pe_s = 2000$ are used. For all cases, $\sigma'_\Gamma = -5000$ is used as discussed in Appendix A. The results given for immobile interfaces are obtained by neglecting the second term in Eq. (36) and the results for the clean interface case stands for $\Gamma_0 = 0$. As the coalescence time of a clean interface with $\lambda^* \leq 0.1$ shown to converge to the $\lambda^* = 0$ case by Ozan and Jakobsen (2019), for both $\lambda^* = 10^{-2}$ and $\lambda^* = 10^{-4}$ the clean interface results are obtained by setting $\lambda^* = 0$ in Eq. (36).

The coalescence time for the systems where $\mu_d \approx \mu_c$ is given as a function of V_{app} and Bo in Figs. 8 and 9, in which $Pe_s = 2.5$ and $Pe_s = 25$, respectively. The results can be broken down into four types of curves: the immobile curves stand for completely immobilized interfaces regardless of the immobilization mechanism, the clean curves stand for an interface without any impurities ($\Gamma_0 = 0$), $Bo = 0$ curves show the individual effect of the Marangoni flow

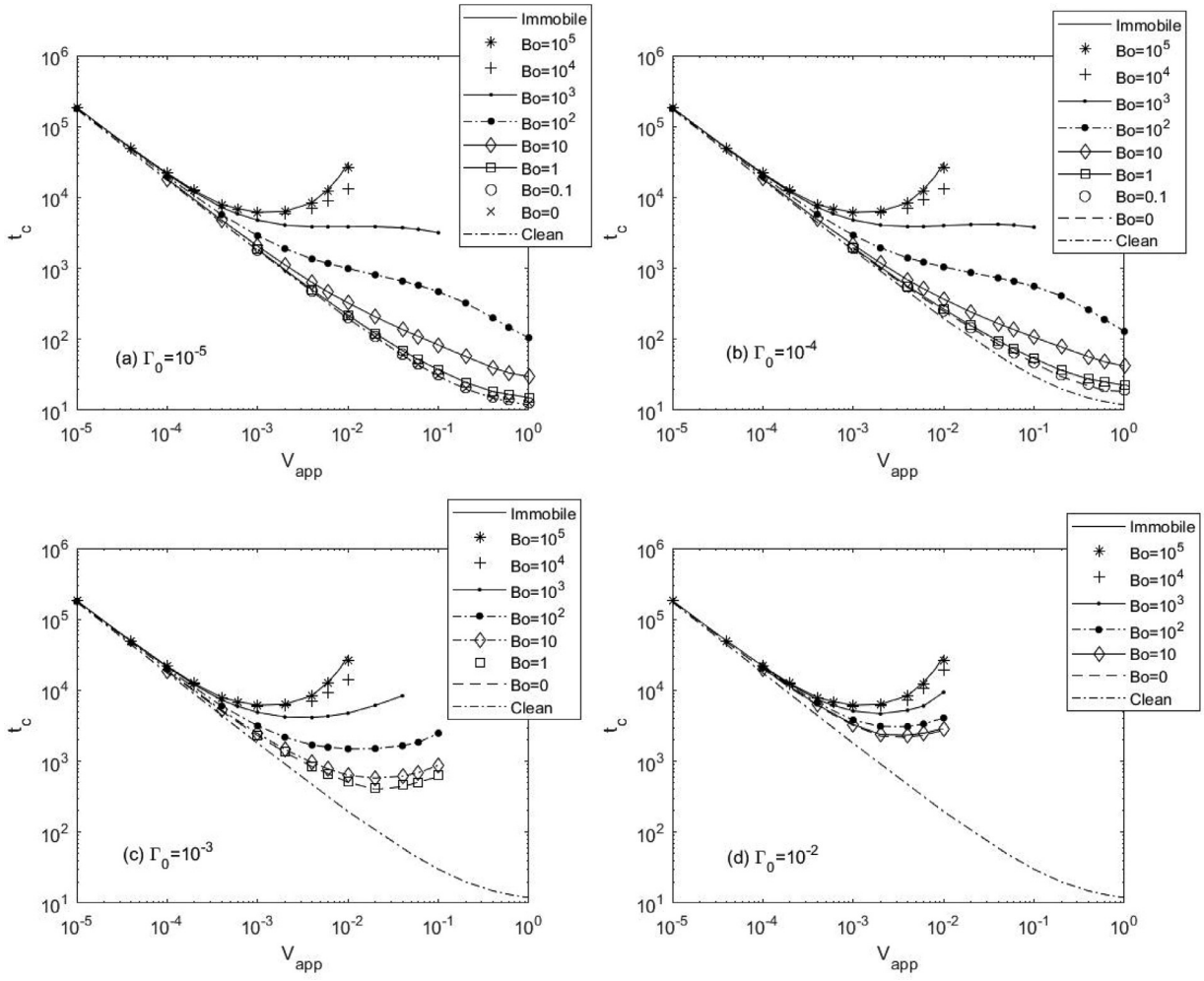

Fig. 9. Coalescence time for $\mu_d \approx \mu_c$ and $Pe_s = 25$ as a function of V_{app} and Bo with (a) $\Gamma_0 = 10^{-5}$, (b) $\Gamma_0 = 10^{-4}$, (c) $\Gamma_0 = 10^{-3}$ and (d) $\Gamma_0 = 10^{-2}$. All results are obtained, $A^* = 10^{-3}$ and $r_\infty = 30$.

since the surface viscosities are neglected, and the curves with non-zero values of Bo are used to examine the effect of the surface viscosities without disregarding the Marangoni flow. In both Figs. 8 and 9, $Bo = 0$ curves reveal that the surface tension gradients changes t_c only when $\Gamma_0 > 10^{-5}$. Furthermore, as Γ_0 increases, the $Bo = 0$ results gradually deviate more and more from the clean interface's, and create up to $1-2$ orders of magnitude difference in t_c at higher approach velocities. Revisiting the tangential stress balance as given by Eq. (37), it can be seen that its second term, which represents the surface tension driven flow, scales with Γ_0 through $\frac{\partial \Gamma}{\partial r}$ (notice that σ'_Γ is a constant). This dependence explains the amplification in the effect of the Marangoni flow with Γ_0. However, a similar discussion on the surface viscosity related terms in the same equation, the first and the third terms, indicates that the effects of the surface viscosities should not scale with the initial condition, since both terms are multiplied by Γ/Γ_0, which cancels the impact of changing Γ_0. Figs. 8(a) and 9(a) show that when the Marangoni flow is insignificant, the coalescence time for the droplets with $Bo > 0.1$ is different than the ones with clean interfaces. This observation together with the conclusion drawn from Eq. (37), implies that for any value of Γ_0 where the Marangoni flow is negligible, i.e. $\Gamma_0 \leq 10^{-5}$, the surface viscosities change t_c noticeably for $Bo > 0.1$. However, this critical value of Bo changes for larger values of Γ_0, as Marangoni flow becomes more influential and begins to compete with the surface viscosities in terms of being the dominant immobilization mechanism. As can be seen in Fig. 8(b)–(d), for $Pe_s = 2.5$, the results of $Bo > [0.01, 0.1, 1]$ differ from the respective coalescence time curve for $Bo = 0$, for $\Gamma_0 = [10^{-4}, 10^{-3}, 10^{-2}]$, meaning that the surface viscosities affect t_c when $Bo/\Gamma_0 > 100$; or from another point of view, the Marangoni flow is the dominant immobilization mechanism when $Bo/\Gamma_0 \leq 100$. Similarly, from Fig. 9(b)–(d), the critical values can be read as $Bo = [0.1, 1, 10]$ for $\Gamma_0 = [10^{-4}, 10^{-3}, 10^{-2}]$ giving the criterion $Bo/\Gamma_0 > 1000$ for $Pe_s = 25$. A more careful inspection of $Bo = 0$ curves at different Pe_s and fixed Γ_0, e.g. a comparison between $Bo = 0$ curves in Figs. 8(c) and 9(c), shows that the effect of the Marangoni flow becomes more significant with Pe_s, and consequently t_c increases. This observation agrees with the conclusion of Alexandrova (2014), where she observes slower drainage rates with increasing Pe_s. As it indicates the strength of the Marangoni flow, a rise in Pe_s also increases the critical ratio of Bo/Γ_0, showing that the surface should be more viscous to be able to change t_c noticeably for larger Pe_s. Finally, in all results, $Bo = 10^5$ is the value at which the interface is completely immobilized. This conclusion agrees with the immobilization condition found in Section 4.2, $Bo\lambda^* \approx 1000$, as $\lambda^* = 10^{-2}$ is employed in the $\mu_d \approx \mu_c$ case.

The dimensionless numbers fed to the solver for the $\mu_d << \mu_c$ case corresponds to the systems with 1 mm bubbles in water. The coalescence time as a function of Bo and V_{app} is given for $Pe_s = 200$ and $Pe_s = 2000$ in Figs. 10 and 11, respectively. The complete immobilization criterion ($Bo\lambda^* \approx 1000$) holds, as t_c converges to the

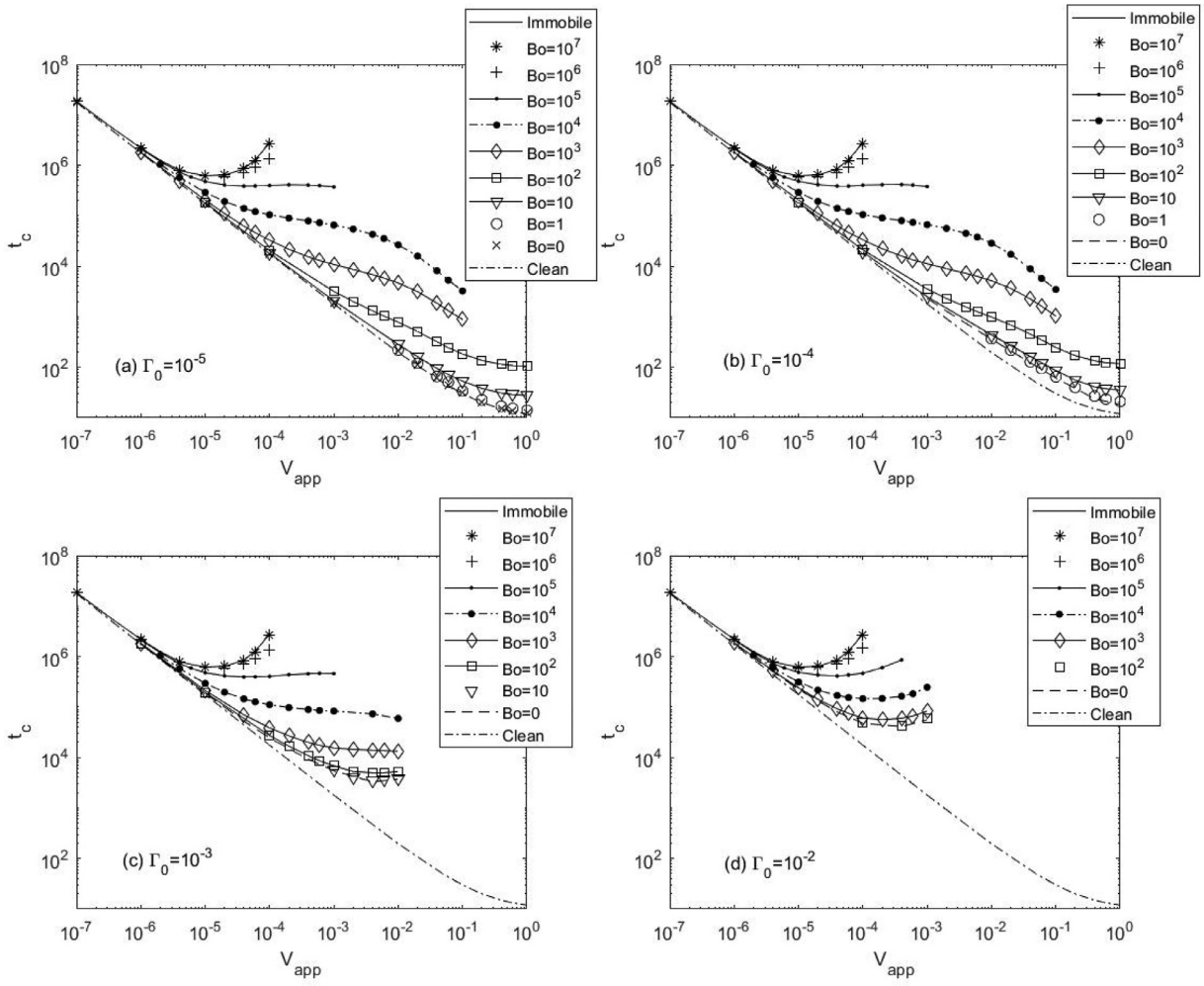

Fig. 10. Coalescence time for $\mu_d << \mu_c$ and $Pe_s = 200$ as a function of V_{app} and Bo with (a) $\Gamma_0 = 10^{-5}$, (b) $\Gamma_0 = 10^{-4}$, (c) $\Gamma_0 = 10^{-3}$ and (d) $\Gamma_0 = 10^{-2}$. All results are obtained, $A^* = 10^{-3}$ and $r_\infty = 30$.

immobile case around $Bo \approx 10^7$ when $\lambda^* = 10^{-4}$. Once again, for both values of Pe_s investigated, the Marangoni flow only affects t_c when $\Gamma_0 \geq 10^{-4}$. From Figs. 10(a) and 11(a), it is seen that when Marangoni flow is negligible, the immobilization due to the surface viscosities starts after $Bo \approx 1$, as the t_c curves after that value deviates from the one for the clean interface. Fig. 10(b)–(d) shows that the surface viscosities has an impact on t_c if $Bo/\Gamma_0 \geq 10^4$, since the results converge to the $Bo = 0$ curves at $Bo = [1, 10, 100]$ respectively when $\Gamma_0 = [10^{-4}, 10^{-3}, 10^{-2}]$; otherwise the Marangoni flow overshadows their effect. Same analysis in Fig. 11 yields the corresponding values as $Bo = [1, 100, 1000]$ for $\Gamma_0 = [10^{-4}, 10^{-3}, 10^{-2}]$. Throughout the study the critical value of $Bo = 1$ for $\Gamma_0 = 10^{-4}$ and $Pe_s = 2000$, is the only exception to the linear relation between the critical Bo and Γ_0. However, it should be noted that our model involves equations with nonlinear terms affected by multiple dimensionless parameters, such as the tangential stress balance, Eq. (37). Therefore, it cannot be claimed the relation between the critical value of Bo and Γ_0 has to be strictly linear, and such exceptions can be encountered.

Using the conclusions of Section 4.2 and the insight obtained from Figs. 8–11, the surface properties/phenomena affecting the coalescence time can be summarized in a map where Γ_0 (or λ^* in $\mu_d >> \mu_c$ case) and Bo are the key parameters determining the behavior. Accordingly, four different regions together with the complete immobilization zones are identified and shown in Fig. 12 for all three viscosity ratio cases discussed in this work. The complete immobilization observed here occurs either due to high dispersed phase viscosity or high surface viscosities. The former is only possible in the high viscosity droplet case when $\lambda^* \geq 100$ regardless of the value of the other parameters, whereas the latter applies to all cases and indicates immobilization when $Bo\lambda^* \geq 1000$. In the first and the second regions, the coalescence time is not affected by the Marangoni flow, since there are either no surface tension gradients present in the system, or they are not large enough. This is due to the uniform concentration distribution in $\mu_d >> \mu_c$ case, and due to low amount of surfactants ($\Gamma_0 \leq 10^{-5}$) in $\mu_d \approx \mu_c$ and $\mu_d << \mu_c$ cases. The surface viscosities, on the other hand, are negligible in the first region, but have noticeable impact on t_c in the second region. The boundary between the first and the second regions seems to be independent of the value of Pe_s in all cases, and also independent of λ^* for high viscosity droplets. In regions three and four, the Marangoni flow becomes significant, whereas the effect of the surface viscosities are only noticeable in the fourth region and negligible in the third. These regions do not exist in the $\mu_d >> \mu_c$ case, since the Marangoni flow is always negligible due to the uniform Γ distribution. The solid lines in Fig. 12(b) and (c) separate regions three and four, and labeled with the corresponding Pe_s values.

By using the numerical values provided in Appendix A, the characteristic scale for the surface viscosities, $\epsilon \mu_d R_p$, can be es-

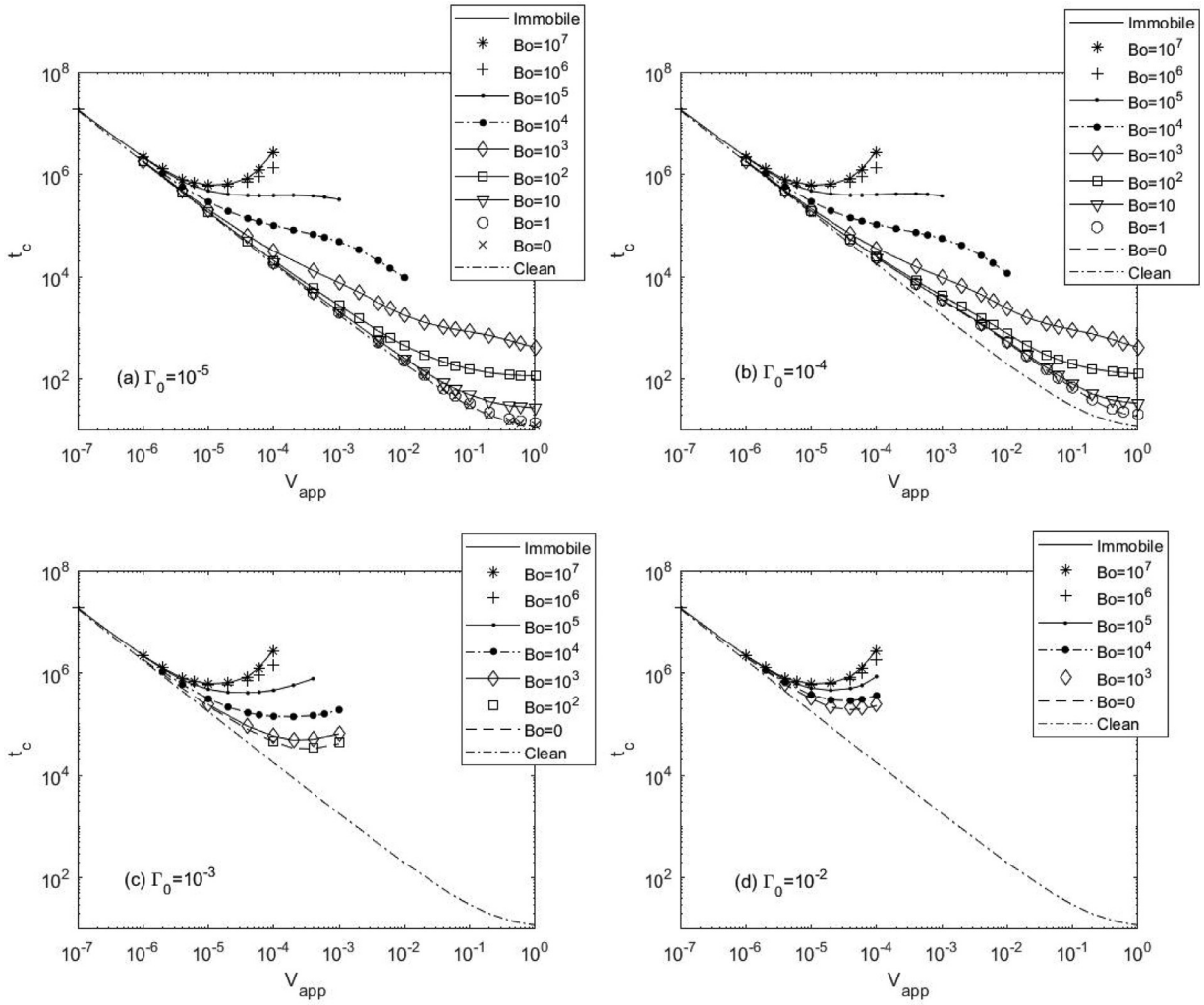

Fig. 11. Coalescence time for $\mu_d << \mu_c$ and $Pe_s = 2000$ as a function of V_{app} and Bo with (a) $\Gamma_0 = 10^{-5}$, (b) $\Gamma_0 = 10^{-4}$, (c) $\Gamma_0 = 10^{-3}$ and (d) $\Gamma_0 = 10^{-2}$. All results are obtained, $A^* = 10^{-3}$ and $r_\infty = 30$.

timated as $5 \times 10^{-6}\, sp$ and $10^{-7}\, sp$ for 1 mm droplets in water ($\mu_d \approx \mu_c$), and for 1 mm air bubbles in water ($\mu_d << \mu_c$), respectively. Here the unit sp stands for surface Poise and equivalent to g/s. These scales can be used to convert Bo into dimensional values of surface viscosities through the definition, $Bo = \frac{\kappa_{I0}+\mu_{I0}}{\epsilon \mu_d R_p}$, where κ_{I0} and μ_{I0} correspond to the initial values of the surface viscosities, i.e., to their values at Γ_0. Then, by converting the dimensionless values separating the first two regions in Fig. 12(b) and (c), it is seen that for $\Gamma_0 \leq 10^{-5}$, the surface viscosities affect t_c only if $\kappa_{I0} + \mu_{I0}$ is larger than $5 \times 10^{-7}\, sp$ and $10^{-7}\, sp$, respectively for $\mu_d \approx \mu_c$ and $\mu_d << \mu_c$ cases. On the other hand, by converting the lines separating regions three and four, a relation based on the ratio of the surface viscosities to the surface excess concentration can be obtained via $Bo/\Gamma_0 = \frac{(\kappa_{I0}+\mu_{I0})/\epsilon \mu_d R_p}{\Gamma_0}$. Notice that, although κ_{I0} and μ_{I0} are dimensional variables, Γ_0 is still scaled by Γ_m. Then, for $\mu_d \approx \mu_c$, the effect of the surface viscosities is significant when $\frac{(\kappa_{I0}+\mu_{I0})}{\Gamma_0} \geq 5 \times 10^{-4}\, sp$ and $\frac{(\kappa_{I0}+\mu_{I0})}{\Gamma_0} \geq 5 \times 10^{-3}\, sp$ for $Pe_s = 2.5$ and $Pe_s = 25$, respectively. Similarly, the limits for $\mu_d << \mu_c$ corresponds to $\frac{(\kappa_{I0}+\mu_{I0})}{\Gamma_0} \geq 10^{-3}\, sp$ and $\frac{(\kappa_{I0}+\mu_{I0})}{\Gamma_0} \geq 10^{-2}\, sp$, when $Pe_s = 200$ and $Pe_s = 2000$. The converted limits can be extrapolated by setting $\Gamma_0 = 1$, only to make a very rough comparison to the experimental values in the literature, to have an idea on whether the values where the surface viscosities are significant according to our simulations, are reasonable or not. $\Gamma_0 = 1$ corresponds to the critical micelle concentration, and most likely is the point where the highest surface viscosities are measured in experiments. Then, by revisiting works of Djabbarah and Wasan (1982) and Ting et al. (1984), it can be seen that the maximum values they observe are $\approx 2\, sp$ and $\approx 0.3\, sp$, respectively. Both values seems to be much larger than all the critical values we observed, showing that the surface viscosities would be crucial in the coalescence of fluid particles with such interfaces. On the other hand, Zell et al. (2014) measure the surface shear viscosities of a soluble surfactant monolayer as below $10^{-5}\, sp$ and that of an insoluble one as $10^{-1}\, sp$, which indicate that the values rendering the surface viscosities non-negligible in coalescence is only achievable for the insoluble surfactant in their work. Another comparison can be done between the $\mu_d \approx \mu_c$ case and the conclusions of Zapryanov et al. (1983). For a liquid-liquid system, they determine the range where the surface viscosities are non-negligible for the film drainage as from $10^{-3}\, sp$ to $1\, sp$, and they claim that the Marangoni flow is always much more influential than the surface viscosities. These values correspond to $Bo = 200$ and $Bo = 2 \times 10^5$, respectively, when $\epsilon \mu_d R_p \approx 5 \times 10^{-6}\, sp$ is taken. The complete immobilization criterion of $Bo \approx 10^5$ for $\mu_d \approx \mu_c$ seem to agree well with their upper limit of $Bo = 2 \times 10^5$, whereas their lower limit is orders of magnitude larger than most of the values separating regions 1 and 2, and regions 3 and 4 in Fig. 12(b). The main reason behind this discrepancy might be their approach in modeling

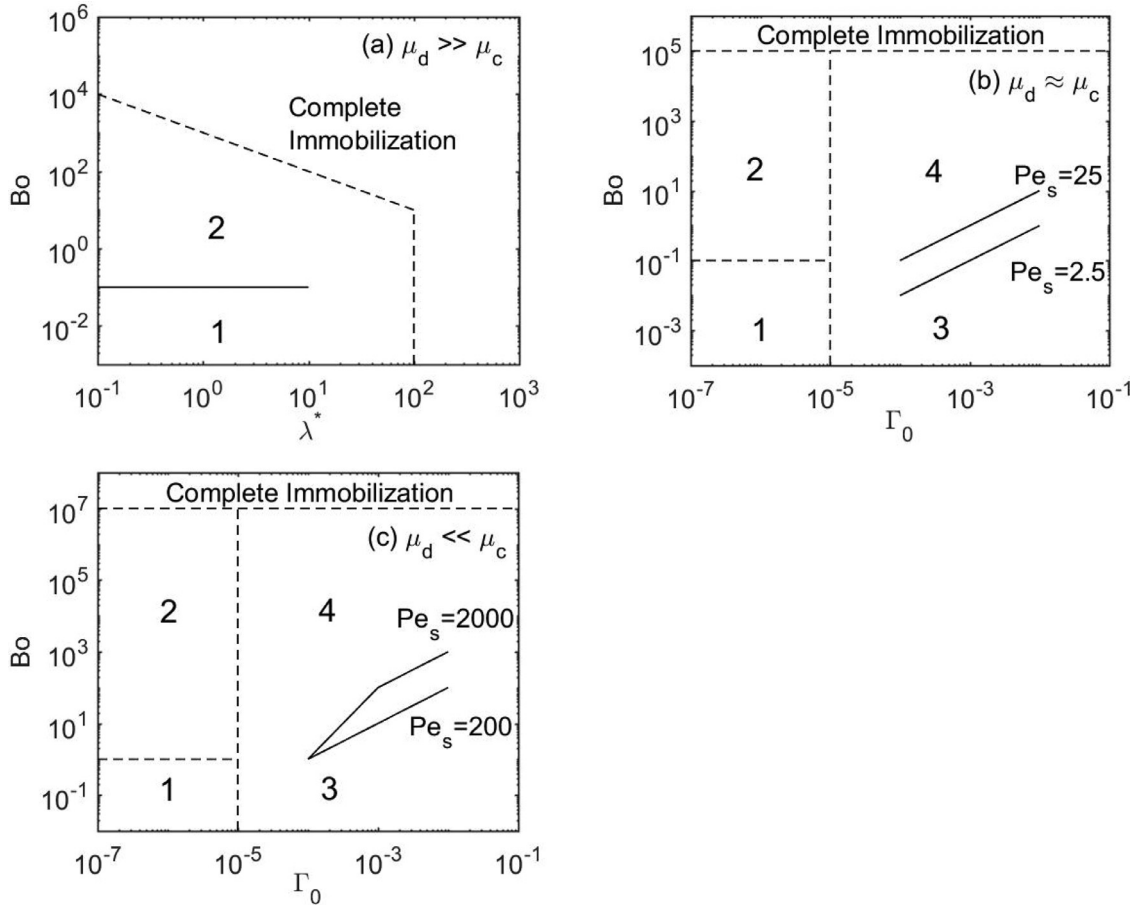

Fig. 12. Regions showing the effect of the surface properties/phenomena on the coalescence time for (a) $\mu_d >> \mu_c$, (b) $\mu_d \approx \mu_c$ and (c) $\mu_d << \mu_c$. In region 1, neither Marangoni flow nor the surface viscosities affect the coalescence time. In region 2, the effect of the surface viscosities is dominant over the Marangoni flow and vice versa in region 3. In region 4, both the Marangoni flow and the surface viscosities have significant impact on the coalescence time.

the interface as being non-deformable. As discussed earlier both surface phenomena promote the dimple formation, which affects the drainage/coalescence behavior dramatically. Therefore, failing to capture interfacial deformations results in underestimation of the role of the surface phenomena, and predicts a higher lower limit. In addition, the current analysis reveals that the Marangoni flow is much more influential than the surface viscosities only in region 3, i.e., only when Bo/Γ_0 is smaller than a certain value. As a final remark, it should be noted that the regions and critical values described in this section are only order of magnitude estimates, which are useful to describe the change in behavior with respect to Bo and Γ_0 (or λ^*), rather than being strictly defined values.

The shape of the t_c curves given in Figs. 8–11 should also be discussed following the framework proposed by Ozan and Jakobsen (2019). Although, all three regimes of coalescence behavior discussed by them are observed in most of the coalescence time curves presented here, in some curves, e.g. $Bo = 10^4$ curve in Fig. 11(b), the third regime in which t_c increases with V_{app} does not exist. Instead, t_c follows a trend with V_{app} that is almost parallel (in log-log scale) to the clean interface curve. The introduction of the surface viscosities might be responsible for the emergence of this new trend, as it is not encountered in any case where the interface is inviscid. For all sets of parameters investigated in Figs. 8–11, it can be seen that $Bo = 0$ curves begin to deviate from linearity at lower V_{app} values as Γ_0 increases, i.e., as Marangoni flow gets stronger. Since this deviation is a result of dimple formation, it can be concluded that the Marangoni flow promotes dimpling of the interface, regardless of the values of Pe_s or λ^*. Similarly, the value of V_{app} at which the deviation starts, seems to decrease with Bo for all values of Pe_s, Γ_0 and λ^* investigated, showing that the surface viscosities also promote dimpling.

5. Conclusions

This work studies the effects of the surface viscosities and the Marangoni stresses on the coalescence behavior and the coalescence time, t_c, via a film drainage model with deformable interfaces obeying the Boussinesq surface fluid model. Based on the dispersed to continuous phase viscosity ratio, the analyses are separated in three cases, where high droplet to water viscosity ratio ($\mu_d >> \mu_c$), comparable droplet to water viscosity ratio ($\mu_d \approx \mu_c$) and gas bubbles in water ($\mu_d << \mu_c$) systems are considered. It is seen that the surface Péclet number, Pe_s, is small enough to guarantee uniform surfactant distribution along the interface only when $\mu_d >> \mu_c$. The uniform distribution indicates that the results are independent of the value of Pe_s, provided that it is small enough. In that case, the surface tension gradients are neglected and only the effect of the surface viscosities is examined via the Boussinesq number, Bo. As Bo increases, the tangential velocity of the interface decreases, consequently the drainage slows down, and t_c increases. In all cases, when $Bo\lambda^* \geq 1000$ the interface appears to be completely immobilized, whereas for $\lambda^* > 100$ the dispersed phase viscosity is large enough to immobilize the interface by itself.

When μ_d is comparable to or lower than μ_c, the surfactant distribution becomes non-uniform creating Marangoni stresses and

surface tension gradient driven flows along the interface. It is concluded that both the Marangoni flow and the surface viscosities have immobilizing effects on the interface, yet they might overshadow each others effect depending on the values of Γ_0, Bo and Pe_s. When, $\Gamma_0 \leq 10^{-5}$, Marangoni flow do not change the coalescence time in any case, and the surface viscosities are only significant in that limit when $Bo \geq 0.1$ and $Bo \geq 1$, respectively for $\mu_d \approx \mu_c$ and $\mu_d << \mu_c$. However, the surface tension gradients get larger as Γ_0 increases, and eventually for $\Gamma_0 \geq 10^{-4}$ the Marangoni flow also starts to affect t_c. Here, the ratio Bo/Γ_0 shows whether the surface viscosities has significant effect on t_c or not. The ratio after which the surface viscosities have noticeable impact on the system are found as $Bo/\Gamma_0 \approx 100$ and $Bo/\Gamma_0 \approx 1000$ for $Pe_s = 2.5$ and $Pe_s = 25$ for $\mu_d \approx \mu_c$, and for the bubble-water system as $Bo/\Gamma_0 \approx 10^4$ and $Bo/\Gamma_0 \approx 10^5$ for $Pe_s = 200$ and $Pe_s = 2000$, respectively. Since Pe_s indicates the magnitude of the surface tension gradients and the strength of the Marangoni flow, as it increases, the critical values of Bo/Γ_0 also increase. Below these limits the Marangoni flow appears to be the only non-negligible surface phenomena. For the liquid-liquid systems, the limit above which the surface viscosities affect the drainage/coalescence shown to be orders of magnitude lower than the previously suggested value of $1\,sp$ by Zapryanov et al. (1983). The interfacial deformations are found to be crucial in understanding the role of the surface phenomena. A comparison between sample calculations based on 1 mm fluid particles and experimental results in the literature indicates that the experimental values of the surface viscosities might fall into the regions where they have significant effects on the coalescence time.

In all cases investigated, the effects of the surface phenomena seems to amplify with the approach velocity. At very low velocities, corresponding to the linear drainage regime, neither the surface viscous nor the Marangoni flows change the coalescence time significantly. However, they both reduce the critical velocity after which dimple formation is observed, i.e., promote the dimple formation at the interface.

Acknowledgements

The work was supported by the Research Council of Norway (Grant no. 267669).

Appendix A

This appendix aims to explain the estimation of the dimensionless parameters used in the simulations. The small parameter ϵ is approximated as 10^{-2}, the viscosity of the continuous phase is taken as $\mu_c = 10^{-3}$ kg/ms to represent water. For $\mu_d >> \mu_c$ case, the dispersed phase is chosen as ten times or more viscous than water, i.e., $\mu_d \geq 10\mu_c$, which corresponds to $\lambda^* = \epsilon \frac{\mu_d}{\mu_c} \geq 0.1$. The case $\mu_d \approx \mu_c$ represents the system of droplets and continuous phase with similar viscosities, and by taking $\mu_c = \mu_d$, the input is determined as $\lambda^* = 10^{-2}$. Finally, $\mu_d << \mu_c$ case stands for gas bubbles in water, therefore the dispersed viscosity is taken as a typical value to represent air, 1.8×10^{-5} kg/ms, and $\lambda^* = 10^{-4}$ is set since it is the order of magnitude of μ_d/μ_c. In the cases where droplets are considered the surface tension is taken as $\sigma_0 = 50 \times 10^{-3}$ kg/s^2, whereas for bubbles it is $\sigma_0 = 72.8 \times 10^{-3}$ kg/s^2. All calculations are done for 1 mm fluid particles, and both the continuous phase and the surface diffusion coefficients, D_c and D_I, are either 10^{-8} m^2/s or 10^{-9} m^2/s. Then, the maximum value of $\epsilon^2 Pe$ appearing in Eq. (31) is

$$\epsilon^2 Pe = \epsilon^6 \frac{R_p \sigma_0}{D_c \lambda^* \mu_c} \approx 3 \times 10^{-5} \frac{1}{\lambda^*} \tag{47}$$

showing that even for the smallest λ^* value used in this work, the term in Eq. (31) can be neglected. The surface Péclet numbers for droplets become

$$Pe_s = \epsilon^4 \frac{R_p \sigma_0}{D_I \lambda^* \mu_c} = 2.5 \times 10^{-10} \frac{1}{D_I \lambda^*} \tag{48}$$

which gives $Pe_s = 2.5$ and $Pe_s = 25$ respectively for $D_I = 10^{-8}\, m^2/s$ and $D_I = 10^{-9}\, m^2/s$ for $\mu_d \approx \mu_c$ ($\lambda^* = 10^{-2}$) case. Similarly for bubbles

$$Pe_s = \epsilon^3 \frac{R_p \sigma_0}{D_I \mu_d} = 2.0 \times 10^{-6} \frac{1}{D_I} \tag{49}$$

estimating $Pe_s = 200$ and $Pe_s = 2000$. Finally, a typical value signifying the dependence of the dimensionless surface tension to dimensionless surface excess concentration, $\frac{\Delta\tilde{\sigma}}{\Delta\tilde{\Gamma}}$ is chosen as -0.5, yielding $\tilde{\sigma}'_{\tilde{\Gamma}} = \epsilon^2 \frac{\Delta\tilde{\sigma}}{\Delta\tilde{\Gamma}} = -5000$ to be used in simulations.

References

Abid, S., Chesters, A.K., 1994. The drainage and rupture of partially-mobile films between colliding drops at constant approach velocity. Int. J. Multiph. Flow 20 (3), 613–629.

Alexandrova, S., 2014. Film drainage and coalescence of drops in the presence of surfactant. J. Chem. Technol. Metall. 49 (4).

Allan, R.S., Charles, G.E., Mason, S.G., 1961. The approach of gas bubbles to a gas/liquid interface. J. Colloid Sci. 16 (2), 150–165.

Bazhlekov, I.B., Chesters, A.K., Van de Vosse, F.N., 2000. The effect of the dispersed to continuous-phase viscosity ratio on film drainage between interacting drops. Int. J. Multiph. Flow 26 (3), 445–466.

Chan, D.Y., Klaseboer, E., Manica, R., 2011. Film drainage and coalescence between deformable drops and bubbles. Soft Matter 7 (6), 2235–2264.

Chesters, A., 1991. Modelling of coalescence processes in fluid-liquid dispersions: a review of current understanding. Chem. Eng. Res. Des. 69 (A4), 259–270.

Chesters, A.K., Hofman, G., 1982. Bubble coalescence in pure liquids. In: In Mechanics and Physics of Bubbles in Liquids. Springer, Dordrecht, pp. 353–361.

Coulaloglou, C.A., 1975. Dispersed phase interactions in an agitated flow vessel. Illinois Institute of Technology, Chicago Ph.d. dissertation.

Davis, R.H., Schonberg, J.A., Rallison, J.M., 1989. The lubrication force between two viscous drops. Phys. Fluids A 1 (1), 77–81.

Del Castillo, L.A., Ohnishi, S., Horn, R.G., 2011. Inhibition of bubble coalescence: effects of salt concentration and speed of approach. J. Colloid Interface Sci. 356 (1), 316–324.

Derjaguin, B.V., Kussakov, M., 1939. Anomalous properties of thin polymolecular films. Acta Physicochim. URSS 10 (1), 25–44.

Djabbarah, N.F., Wasan, D.T., 1982. Dilational viscoelastic properties of fluid interfaces–III mixed surfactant systems. Chem. Eng. Sci. 37 (2), 175–184.

Edwards, D.A., Brenner, H., Wasan, D.T., 1991. Interfacial Transport Processes and Rheology. Butterworth-Heinemann.

Howarth, W.J., 1964. Coalescence of drops in a turbulent flow field. Chem. Eng. Sci. 19 (1), 33–38.

Johns, L.E., Narayanan, R., 2007. Interfacial instability. Springer Science & Business Media.

Kirkpatrick, R.D., Lockett, M.J., 1974. The influence of approach velocity on bubble coalescence. Chem. Eng. Sci. 29 (12), 2363–2373.

Klaseboer, E., Chevaillier, J.P., Gourdon, C., Masbernat, O., 2000. Film drainage between colliding drops at constant approach velocity: experiments and modeling. J. Colloid Interface Sci. 229 (1), 274–285.

Ladyzhenskaya, O.A., 1969. The Mathematical Theory of Viscous Incompressible Flow (Vol. 76). Gordon and Breach, New York.

Lee, J.C., Hodgson, T.D., 1968. Film flow and coalescence-i basic relations, film shape and criteria for interface mobility. Chem. Eng. Sci. 23 (11), 1375–1397.

Lehr, F., Millies, M., Mewes, D., 2002. Bubble-size distributions and flow fields in bubble columns. AIChE J. 48 (11), 2426–2443.

Li, D., 1996. Coalescence between small bubbles: effects of surface tension gradient and surface viscosities. J. Colloid Interface Sci. 181 (1), 34–44.

Liao, Y., Lucas, D., 2010. A literature review on mechanisms and models for the coalescence process of fluid particles. Chem. Eng. Sci. 65 (10), 2851–2864.

Maru, H.C., Wasan, D.T., 1979. Dilational viscoelastic properties of fluid interfaces-II: experimental study. Chem. Eng. Sci. 34 (11), 1295–1307.

Orvalho, S., Ruzicka, M.C., Olivieri, G., Marzocchella, A., 2015. Bubble coalescence: effect of bubble approach velocity and liquid viscosity. Chem. Eng. Sci. 134, 205–216.

Ozan, S.C., Jakobsen, H.A., 2019. On the effect of the approach velocity on the coalescence of fluid particles. Int. J. Multiph. Flow 119, 223–236.

Pintar, A.J., Israel, A.B., Wasan, D.T., 1971. Interfacial shear viscosity phenomena in solutions of macromolecules. J. Colloid Interface Sci. 37 (1), 52–67.

Ponce-Torres, A., Montanero, J.M., Herrada, M.A., Vega, E.J., Vega, J.M., 2017. Influence of the surface viscosity on the breakup of a surfactant-laden drop. Phys. Rev. Lett. 118 (2), 024501.

Pozrikidis, C., 1992. Boundary Integral and Singularity Methods for Linearized Viscous Flow. Cambridge University Press.

Saboni, A., Gourdon, C., Chesters, A.K., 1995. Drainage and rupture of partially mobile films during coalescence in liquid-liquid systems under a constant interaction force. J. Colloid Interface Sci. 175 (1), 27–35.

Scheid, B., Delacotte, J., Dollet, B., Rio, E., Restagno, F., Van Nierop, E.A., Cantat, I., Langevin, D., Stone, H.A., 2010. The role of surface rheology in liquid film formation. EPL (Europhys. Lett.) 90 (2), 24002.
Shen, L., Denner, F., Morgan, N., van Wachem, B., Dini, D., 2018. Capillary waves with surface viscosity. J. Fluid Mech. 847, 644–663.
Shinnar, R., 1961. On the behaviour of liquid dispersions in mixing vessels. J. Fluid Mech. 10 (2), 259–275.
Shinnar, R., Church, J.M., 1960. Statistical theories of turbulence in predicting particle size in agitated dispersions. Industrial Eng. Chem. 52 (3), 253–256.
Ting, L., Wasan, D.T., Miyano, K., Xu, S.Q., 1984. Longitudinal surface waves for the study of dynamic properties of surfactant systems. II. air-solution interface. J. Colloid Interface Sci. 102 (1), 248–259.
Trefethen, L.N., 2000. Spectral methods in MATLAB (Vol. 10). Siam.
Yiantsios, S.G., Davis, R.H., 1991. Close approach and deformation of two viscous drops due to gravity and van der waals forces. J. Colloid Interface Sci. 144 (2), 412–433.
Zapryanov, Z., Malhotra, A.K., Aderangi, N., Wasan, D.T., 1983. Emulsion stability: an analysis of the effects of bulk and interfacial properties on film mobility and drainage rate. Int. J. Multiph. Flow 9 (2), 105–129.
Zell, Z.A., Nowbahar, A., Mansard, V., Leal, L.G., Deshmukh, S.S., Mecca, J.M., Christopher, J.T., Squires, T.M., 2014. Surface shear inviscidity of soluble surfactants. Proc. Natl. Acad. Sci. 111 (10), 3677–3682.